



UNDERWATER SIMULATION AND MAPPING USING IMAGING SONAR THROUGH RAY THEORY AND HILBERT MAPS

Eduardo Elael de Melo Soares

Dissertação de Mestrado apresentada ao Programa de Pós-graduação em Engenharia Elétrica, COPPE, da Universidade Federal do Rio de Janeiro, como parte dos requisitos necessários à obtenção do título de Mestre em Engenharia Elétrica.

Orientador: Ramon Romankevicius Costa

Rio de Janeiro
Março de 2017

UNDERWATER SIMULATION AND MAPPING USING IMAGING SONAR
THROUGH RAY THEORY AND HILBERT MAPS

Eduardo Elael de Melo Soares

DISSERTAÇÃO SUBMETIDA AO CORPO DOCENTE DO INSTITUTO
ALBERTO LUIZ COIMBRA DE PÓS-GRADUAÇÃO E PESQUISA DE
ENGENHARIA (COPPE) DA UNIVERSIDADE FEDERAL DO RIO DE
JANEIRO COMO PARTE DOS REQUISITOS NECESSÁRIOS PARA A
OBTENÇÃO DO GRAU DE MESTRE EM CIÊNCIAS EM ENGENHARIA
ELÉTRICA.

Examinada por:

Prof. Ramon Romankevicius Costa, D.Sc.

Prof. Alessandro Jacoud Peixoto, D.Sc.

Prof. Antonio Candea Leite, D.Sc.

Prof. Paulo César Pellanda, Dr. ENSAE

RIO DE JANEIRO, RJ – BRASIL
MARÇO DE 2017

Soares, Eduardo Elael de Melo

Underwater Simulation and Mapping using Imaging Sonar through Ray Theory and Hilbert Maps/Eduardo Elael de Melo Soares. – Rio de Janeiro: UFRJ/COPPE, 2017.

IX, 70 p.: il.; 29,7cm.

Orientador: Ramon Romankevicius Costa

Dissertação (mestrado) – UFRJ/COPPE/Programa de Engenharia Elétrica, 2017.

Bibliografia: p. 63 – 70.

1. Sonar. 2. 3D Mapping. 3. Simulation.
4. Underwater. I. Costa, Ramon Romankevicius.
- II. Universidade Federal do Rio de Janeiro, COPPE, Programa de Engenharia Elétrica. III. Título.

Resumo da Dissertação apresentada à COPPE/UFRJ como parte dos requisitos necessários para a obtenção do grau de Mestre em Ciências (M.Sc.)

UNDERWATER SIMULATION AND MAPPING USING IMAGING SONAR THROUGH RAY THEORY AND HILBERT MAPS

Eduardo Elael de Melo Soares

Março/2017

Orientador: Ramon Romankevicius Costa

Programa: Engenharia Elétrica

O mapeamento, às vezes como parte de um sistema SLAM, é um tema de pesquisa ativo e tem soluções notáveis usando scanners a laser, mas a maioria do mapeamento subaquático é focada em mapas 2D, que tratam o ambiente como uma planta, ou mapas 2.5D do fundo do mar .

A razão para a dificuldade do mapeamento subaquático origina-se no seu sensor, i.e. sonares. Em contraste com lasers (LIDARs), os sonares são sensores imprecisos e com alto nível de ruído. Além do seu ruído, os sonares do tipo *imaging* têm um feixe sonoro muito amplo e, com isso, efetuam uma medição volumétrica, ou seja, sobre todo um volume.

Na primeira parte dessa dissertação se desenvolve um simulador para sonares do tipo *imaging* de feixe único de alta frequência capaz de replicar os efeitos típicos de multicaminho, ganho direcional e ruído de fundo em ambientes arbitrários. O simulador implementa um método baseado na teoria geométrica de raios, com todo seu desenvolvimento partindo da acústica subaquática.

Na segunda parte dessa dissertação, o simulador é incorporado em um algoritmo de reconstrução de mapas contínuos baseado em *Hilbert Maps*. *Hilbert Maps* surge como uma técnica de aprendizado de máquina sobre espaços de Hilbert, usando mapas de características, aplicadas ao contexto de mapeamento. A incorporação de uma resposta de sonar em um tal mapa é uma contribuição desse trabalho.

Uma comparação qualitativa entre o ambiente de referência fornecido ao simulador e o mapa reconstruído pela técnica proposta, revela *Hilbert Maps* como uma técnica promissora para mapeamento através de sensores ruidosos e, também, aponta para algumas características do ambiente difíceis de se distinguir, e.g. cantos e regiões não suaves.

Abstract of Dissertation presented to COPPE/UFRJ as a partial fulfillment of the requirements for the degree of Master of Science (M.Sc.)

UNDERWATER SIMULATION AND MAPPING OF IMAGING SONAR THROUGH RAY THEORY AND HILBERT MAPS

Eduardo Elael de Melo Soares

March/2017

Advisor: Ramon Romankevicius Costa

Department: Electrical Engineering

Mapping, sometimes as part of a SLAM system, is an active topic of research and has remarkable solutions using laser scanners, but most of the underwater mapping is focused on 2D maps, treating the environment as a floor plan, or on 2.5D maps of the seafloor.

The reason for the problematic of underwater mapping originates in its sensor, i.e. sonars. In contrast to lasers (LIDARs), sonars are unprecise high-noise sensors. Besides its noise, imaging sonars have a wide sound beam effectuating a volumetric measurement.

The first part of this dissertation develops an underwater simulator for high-frequency single-beam imaging sonars capable of replicating multipath, directional gain and typical noise effects on arbitrary environments. The simulation relies on a ray theory based method and explanations of how this theory follows from first principles under short-wavelegnth assumption are provided.

In the second part of this dissertation, the simulator is combined to a continous map algorithm based on Hilbert Maps. Hilbert maps arise as a machine learning technique over Hilbert spaces, using features maps, applied to the mapping context. The embedding of a sonar response in such a map is a contribution.

A qualitative comparison between the simulator ground truth and the reconstructed map reveal Hilbert maps as a promising technique to noisy sensor mapping and, also, indicates some hard to distinguish characteristics of the surroundings, e.g. corners and non smooth features.

Contents

List of Figures	viii
1 Introduction	1
1.1 Purpose and Significance	2
1.2 Objectives	2
1.3 Methodology	3
1.4 Work Structure	3
2 Sonar Simulation	4
2.1 Sonar	4
2.1.1 Physics of Sound	5
2.1.2 Sonar Principle of Operation	6
2.1.3 Available Models	11
2.2 Simulation	12
2.2.1 Techniques Overview	12
2.2.2 Ray Theory	21
2.3 Environment	30
2.3.1 Modeling	30
2.3.2 Characterization	32
2.4 Implementation	33
2.4.1 Algorithm	33
2.4.2 Results	36
3 Mathematical Preliminaries	39
3.1 Hilbert Space	39
3.2 RKHS - Reproducing Kernel Hilbert Space	41
3.2.1 The Evaluation Functional	41
3.2.2 Reproducing Kernels	42
3.2.3 Feature Maps	44
3.3 Probabilistic Regression	44
3.3.1 Binary Logistic Regression	45

3.3.2	Regression on Hilbert Spaces	46
4	Mapping	47
4.1	Map Representation	47
4.1.1	Discrete Map	48
4.1.2	Map of Features	50
4.1.3	Continuous Map	51
4.2	Inverse Sonar Model	53
4.2.1	Sonar on Feature Maps	53
4.3	Map Learning	54
4.3.1	Stochastic Gradient Descent - SGD	54
4.4	Implementation	55
4.4.1	Algorithm	55
4.4.2	Results	56
5	Conclusion	61
5.1	Future Works	62
	Bibliography	63

List of Figures

2.1	Depiction of the working principle of an <i>active sonar</i> . The red speaker-like object represents the transducer, responsible for emitting and receiving the acoustic wave.	7
2.2	Visualization of a multipath for a high frequency short pulse (much smaller than delay times). Black vectors show the path taken by the sound wave. Red dashed vector shows the calculated distance by equation (2.7).	8
2.3	Resolution as the minimum discernible distance between echos.	9
2.4	Far field beam shape and its <i>beamwidth</i> (in blue).	10
2.5	Incident and reflected rays with respective angles.	23
2.6	Scattering reflection weighted.	24
2.7	BRDF and BTDF for transmitted, reflected and scattered rays. (©User:Jurohi / Wikimedia Commons / CC-BY-SA-3.0)	26
2.8	The source E and the virtual sources E', E'_1, E'_2, E'_3 . In this case, E'_3 is not a visible virtual source.	27
2.9	Source on a perfect tiling. The simple pattern facilitates computation.	27
2.10	A 2D view of a pyramidal beam tracing.	28
2.11	Materials reflective characteristics from MILLER [29].	33
2.12	Example of an array for a bearing direction. Actual arrays are longer, depending on resolution.	34
2.13	Overview of the simulation algorithm.	35
2.14	Ray Tracing: Red lines are specular reflections, green lines are diffuse backscattering.	36
2.15	Sonar simulation for the box-like scene.	37
2.16	Sonar simulation for the complex scene.	38
4.1	Mapping with 10% of available beams.	57
4.2	Mapping with 30% of available beams.	58
4.3	Mapping with 100% of available beams, with double pass over samples.	59
4.4	Mapping using only 1 position and 3 sonar orientations, with different number of used beams.	60

5.1	Mapping using only 1 position and 3 sonar orientations with ground truth as green lines.	61
5.2	Blue region is the half probability region and green lines represent ground truth.	62

Chapter 1

Introduction

Underwater mapping and simulation are dual processes; while the latter produce sonar responses for a given environment, the former use these responses to infer the surroundings. As such, simulation is a flexible way of generating data with a known ground truth to test a mapping algorithm. However, to achieve a correct underwater simulation algorithm, simplifying assumptions on sound physics and environmental characteristics are necessary, as well as a definition of the sonar type being modeled.

Profiling and imaging sonars are two classes of sonars whose differences lie in the aperture of their sound beams. Profiling sonars have a narrow sound beam and they are considered the laser scanner analog for underwater mapping, even though profilings still have much wider beam than lasers. The simplest approaches to underwater 3D mapping focus on applying laser scanner techniques to profiling sonars, e.g. point cloud reconstruction. On the other hand, imaging sonars are usually cheaper and have a wider sound beam, covering more space at the expense of having a more ambiguous response. Thus, the choice of using imaging sonars for mapping comes with the challenge of overcoming their measurement uncertainties.

Besides stipulating a sonar type, the meaning of mapping ought to be narrowed down. It is possible to generically define mapping as the process of gathering multiple sensor data to characterize the surroundings. However, how this characterization might be represented depends on the application.

A SLAM (**S**imultaneous **L**ocalization and **M**apping) [1] system has no intrinsic need for a human readable map. In such a system, it could be interesting to store the map information only through its most representative features, but even for SLAM that is not always the case. It is often implemented as a grid with empty/full cells or even as a continuous map.

The mapping of underwater environments is not just a part of a SLAM system. It has importance on its own, it can be used for humans to visualize things that could not be seeing otherwise. If the map is to be seen by a human it should store and merge information about the environment, so that it can be displayed as the

usual map, 3D or 2D depending on the case. This representation also guides how the data could be stored, e.g. if it wants to show a surface, it can be stored as an elevation map, or if one wants to see a 3D object it can be stored as a point cloud, a 3D grid, a continuous map, etc.

1.1 Purpose and Significance

In the ROSA (*Robô para Operações de Stoplogs Alagados*) project, developed by LEAD/COPPETEC for ESBR (Energia Sustentável do Brasil), one of the goals is to make a reconstruction of the hydroelectric power plant turbine entrance. It should spot any underwater debris that could block the lowering of stoplogs¹ and cause delays or even accidents. Interestingly, the stoplog setup has characteristics that make it appropriate for sonar mapping. It has a lifting beam for inserting stoplogs into water that can act as stable fixation point for any sonar structure and provide a good means of localization. Well placed high-end sonars could probably scan such an environment, but they are expensive.

Mechanical imaging sonar is a more affordable type of sonar, however it suffers from imprecise measurements caused by its wide sound beam. This work aims to provide a method to map an environment using imaging sonars. It extends a recent developed continuous map technique (Hilbert maps [2]) by applying it to sonar responses. Continuous maps are techniques that do not discretize the space *a priori* to create a map and, among them, Hilbert maps is an easier to implement method that possesses a high noise immunity. It also implements a simulator with a trade-off between having simplifying assumptions and being as complete as possible for imaging sonars, justifying the choices based on first physical principles and other advanced simulation techniques.

1.2 Objectives

The objectives of this work are the development of a simulator and a mapping system for mechanical imaging sonars, thus being able to validate the hypothesis that these sonars can be used for mapping. The simulator will be able to receive a description of a general environment and calculate the expected response of a high-frequency imaging sonar. Its output shall exhibit common sonar features as multipath effects, noise and beamwidth uncertainty. The response will be presented as polar plot similar to those used by real sonars.

The mapping system will receive sonar measurements, typically the simulator's

¹long rectangular timber beams stacked to block water flow.

output, and generate a Hilbert map representation of the continuous occupancy map, by apply a simple embedding of sonar response method envisioned by the author. The map has to match to the simulator ground truth avoiding inconsistencies caused by the sonar's wide beam. The Hilbert map representation is, technically, just a vector that encodes 3D occupancy maps, however the information of this 3D map will be displayed as 2D cross-sections for better readability.

1.3 Methodology

This work is divided into two parts.

The sonar model definition starts with a compilation on the description of sonar, physical properties of sound waves in water, reflection, sonar directional gain and sources of noise. Those are used to select a simulation technique and model two different environment, a simple and a complex structure, one to feed the mapping algorithm and another to explore more advanced acoustic features, e.g. multipath, directional gain. The simulation results for both environments are then analyzed for those typical sonar features.

The second part is related to mapping. An introductory chapter presents the mathematical concepts used, followed by another with discussions on the difficulties of 3D reconstruction and its methods. The latter includes description of the most common and standard state-of-the-art techniques, with comments on some alternative works, and deeper details of Hilbert maps. Hilbert maps implementation and results, for one of the simulated environments, are displayed at the end of the chapter.

1.4 Work Structure

Chapter 1 Motivation and general description of the thesis.

Chapter 2 Description of sonar models and their working principle. Development of simulation logic from acoustics. Review of simulations techniques on the literature. Implementation and results of a simulator based on a ray theory algorithm.

Chapter 3 Presentation of the mathematical structure necessary for understanding Hilbert Maps.

Chapter 4 Review of mapping techniques on the literature. Detailed description of Hilbert Maps and a proposal of sonar response embbeding. Implementation and results for a box-like environment, from a simulation of chapter 2.

Chapter 5 Comparison between simulation ground truth and reconstructed environment. Suggestion of next steps to improve both simulation and mapping.

Chapter 2

Sonar Simulation

If you cause your ship to stop, and place the head of a long tube in the water and place the outer extremity in your ear, you will hear ships at a great distance from you.

Leonardo Da Vinci, 1490

The idea behind simulation is to have a flexible environment where the system (e.g. sonar, reconstruction model) can be tested on a variety of conditions and the ground truth is well known. It is a mature and widespread mechanism for development of new sonar technologies [3].

Opening this chapter, it will be presented physical foundations behind sonars, the existing technologies, and models. Followed by a rich description of sonar simulation techniques, especially of ray theory based ones, and ending with characterization of the envisioned environment and implementation.

2.1 Sonar

Throughout this thesis one specific type of sonar will be considered, the mechanical imaging active sonar (Section 2.1.3). Sonars have a common underlying principle of operation, but vary greatly on application and hardware constitution.

Sonars are, in some sense, the acoustic analog of a camera. They use sound, instead of light, to capture information about the environment. Hence, to better understand *how* they operate and *what* they are used for, it is important to have a clear concept of sound.

2.1.1 Physics of Sound

The phenomenon that humans perceive as sound is a pressure wave which amplitude exceeds the mean pressure of the medium [4]. It can be referred to as *compressional* or *longitudinal* waves, contrasting with *transversal waves*. The difference between these two kinds of waves relies on the direction of the movement of the particles, being parallel or perpendicular to the propagation of the wave, respectively [5].

On the particular, but common, condition of low energy phenomena [6] (with some other suitable requirements¹) the pressure perturbation wave can be described as the *D'Alembert equation*

$$\nabla^2 \Phi - \frac{1}{c_0^2} \frac{\partial^2}{\partial t^2} \Phi = 0, \quad (2.1)$$

where c_0 is the local sound speed and Φ is the velocity potential, a scalar field that helps describing the sound propagation. Its relation to sound pressure is

$$p = -\rho \frac{\partial}{\partial t} \Phi,$$

which can be directly described as:

$$\nabla^2 p - \frac{1}{c_0^2} \frac{\partial^2}{\partial t^2} p = 0, \quad (2.2)$$

where p is the pressure deviation from the mediums, ρ the density and ∇^2 stands for the Laplace operator. These equations are only valid in free space (no source), however discrete variations of the medium are treated as boundary conditions, giving origin to reflection and refraction.

Besides pressure, sound has another important derived property: intensity. Much as the case of electromagnetic waves, sound intensity (or acoustic intensity) measures the mean value of the sound energy flux (i.e. energy rate per area):

$$\vec{I} = \overline{p\vec{v}}, \quad (2.3)$$

where \vec{I} represents the *acoustic intensity* vector, \vec{v} the *acoustic velocity* (i.e. the velocity of a particle in the medium) and overline (e.g. $\overline{p\vec{v}}$) the mean over some time period. The *acoustic velocity* can also be derived from the velocity potential Φ as:

$$\vec{v} = \nabla \Phi.$$

When considering a wave far from its source, solutions to the equation (2.2) give rise to a *plane wave* (where the coherent wave front propagate in a plane). It makes clear the relationship between \vec{v} and p :

¹A perfect simple fluid in an initial state of stationary homogeneous equilibrium

$$\vec{v} = \frac{p}{\rho c_0} \vec{n}_0 ,$$

where \vec{n}_0 is the unit normal vector to the wavefront. Plugging it back to (2.3):

$$\vec{I} = \frac{1}{\rho c_0} \overline{p^2} \vec{n}_0 . \quad (2.4)$$

This equation shows the proportionality between the *acoustic intensity* and the mean of the square of the pressure. The inverse of the proportionality constant ρc_0 is called the *characteristic impedance* because it measures the degree of “resistance to propagation” of the medium.

Because the acoustic intensity (and related quantities) varies in orders of magnitude while propagating, it is common to quantify it on a logarithmic scale, specifically *decibels* (dB) [7]:

$$I_{dB} = 10 \log_{10} \left(\frac{I}{I_0} \right) . \quad (2.5)$$

Here, I_{dB} is the intensity measured in *decibels*, I is the intensity value and I_0 a reference intensity values, usually defined somewhere near the source. In the case of reflected/refracted wave, I_0 may also refers to the intensity of the incoming wave. A direct relation between the magnitude of intensity and pressure is found by applying equation (2.4) on equation (2.5):

$$I_{dB} = 20 \log_{10} \left(\frac{p_{rms}}{p_0} \right) , \quad (2.6)$$

where p_{rms} is the *rms* (Root mean squared) value of the wave’s pressure ($\sqrt{\overline{p^2}}$) and p_0 is a pressure value of reference, for underwater acoustics this value is the micro Pascal ($p_0 = 1 \mu\text{Pa}$) [7].

2.1.2 Sonar Principle of Operation

The name Sonar (*Sound Navigation And Ranging*) was originally conceived for any technique that uses acoustic waves on water for navigation, communication and detection, but nowadays it is also used for the equipment that generate/receive these sound waves.

The history of sonar is considered as having began on the year of 1490 through the statement of Leonardo Da Vinci aforementioned on the epigraph of this chapter [8]. That was the birth of *passive sonar*’s technology, where the objective is to listen (receive and process sound waves) the noise from ships, animals and other objects in an attempt to detect and recognize its origin.

However, as it is not expected that all surfaces emit noise, this passive type of

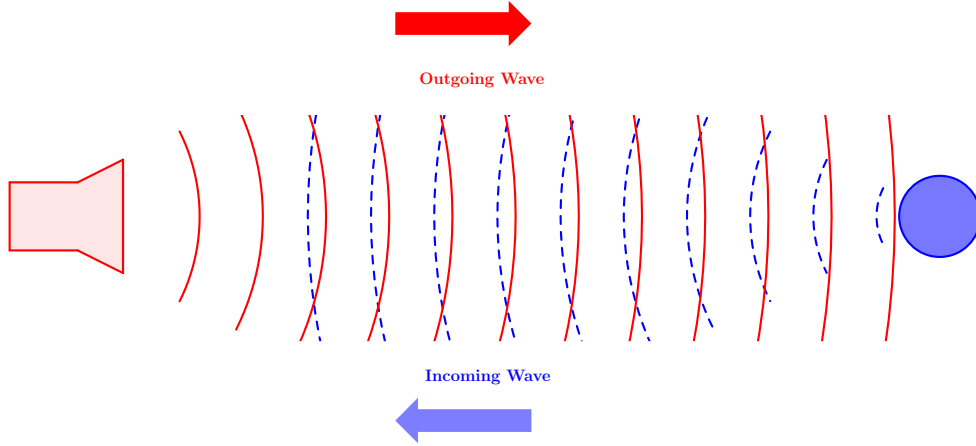


Figure 2.1: Depiction of the working principle of an *active sonar*. The red speaker-like object represents the transducer, responsible for emitting and receiving the acoustic wave.

sonar is not suitable for mapping. For that purpose, another type of sonar that could probe the surrounds had to be devised, those would be called *active sonars*.

Active Sonar

The concept of an *active sonar*, one that emits a sound wave and detects its return (as in Figure 2.1), is much recent. The loss of the *HMS Titanic* due to a collision with an iceberg during its first voyage on April 15 of 1912 [9] fostered the development of a sonar to detect objects kilometers away. Also, during World War I, Allied shipping losses to U-boat attacks further stimulated advances on techniques for uncovering of submerged enemies.

Active sonars are ranging sensor and the way they infer distance is by measuring the time between the emission and reception of an acoustic pulse (a time bounded sound wave) like on (2.1). Given the mean sound speed of the medium throughout the path traveled by the pulse, one can infer range [7]:

$$R = \frac{c_0 \Delta t}{2}, \quad (2.7)$$

where R is the distance between the source and the target, c_0 is the mean sound speed, Δt is the delay between pulse emission and reception, and the denominator 2 is a consequence of time measuring the two way trip of the pulse. When the medium cannot be considered homogeneous, as in long distance travels in the ocean, additional effects must be taken into account [3] (e.g. medium stratification).

Active sonars outputs is influenced by various factors, some considered to be more relevant will be further explored in this section: multipaths, spatial resolution,

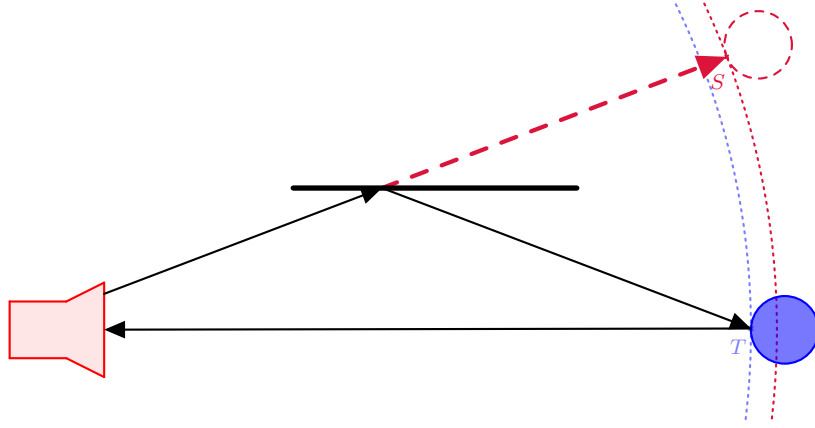


Figure 2.2: Visualization of a multipath for a high frequency short pulse (much smaller than delay times). Black vectors show the path taken by the sound wave. Red dashed vector shows the calculated distance by equation (2.7).

bearing indistinguishability and propagation loss compensation (TVG).

Multipath

Besides sound speed variation, another common issue is *multipath*. The moment a sound wave encounters an interface (e.g. an obstacle like the sea floor or the water surface), it does not fully bounce back to the source, it also undergoes reflection in other directions. Thus, an echo that has traveled a longer path may also arrive, causing a naive application of equation (2.7) to predict the presence of an object further away (Figure 2.2). For low-frequency stable signals, the contribution of all multipaths creates an interference pattern [7], a fact that will not be further explored.

Sonar Resolution and CHIRP Pulses

The minimum distance (or echo delay) that can be resolved by the sonar, depends on the type of pulse emitted (Figure 2.3). There are two main types of pulse: *single frequency* and *chirp* [10, 11]. Some sonars use dual frequency to overcome the trade-off between reach and resolution, given that low-frequency has a longer range and high-frequency a better resolution.

For single frequency sonar, the limit resolution (δR) depends directly on the pulse length (ΔL):

$$\delta R = \frac{c_0 \Delta L}{2}.$$

However, that limitation can be overcome by the use of pulse compression (a cross-correlation filter like matched filters). In this case, a linear varying frequency signal (chirp), or similar multifrequency systems, has its resolution related to the

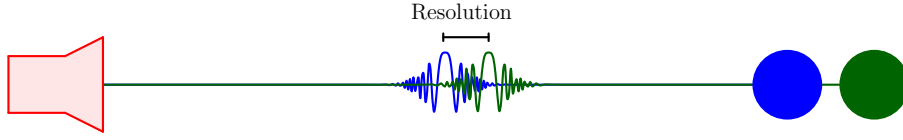


Figure 2.3: Resolution as the minimum discernible distance between echos.

bandwidth (ΔBW):

$$\delta R = \frac{c_0}{2 \Delta BW} .$$

Bearing

The direction where the echo comes from cannot be directly obtained using only one hydrophone (underwater sound transducer). There are two main elements to consider for bearing estimation: *beamwidth* and *hydrophone arrays*.

The majority of simple sonars have only one hydrophone acting as source and receiver. They cannot distinguish the direction of the incoming wave. It is possible to use its *beamwidth* to narrow down the region of the echo origin, being necessary to rotate the transducer in order to capture other directions.

The beam shape of a hydrophone is its directional gain, i.e. the ratio between the intensity of the emitted signal, in a given direction, and the maximum intensity. It also acts as proportional loss of intensity when measuring the received signal incoming from some direction. The concept of a 2-way beam shape follows directly as the net result of transmission and reception. Mathematically, it results in squaring the beam shape. All these concepts are meaningful only if sufficiently far from the source, a region called far field [12].

The *beamwidth*, in turn, is a simplifying concept. The conventional definition is the point where intensity reaches 70% of its peak value, or -3dB . The 2-way beam shape reduces the *beamwidth* to about 72% w.r.t. the 1-way beam beamwidth. If the diameter (D) of the transducer is large compared to the acoustic wavelength (λ), the *beamwidth* (β) can be approximated as:

$$\beta \approx \sin^{-1} \left(\frac{\lambda}{D} \right) .$$

On the other hand, there are hydrophone arrays that can infer the sound direction by relating the spacing between the transducers with the signal difference received by each of them [13, 14]. One technique is very similar to *multilateration*, simply compute the distance measured by each transducer and use this information to

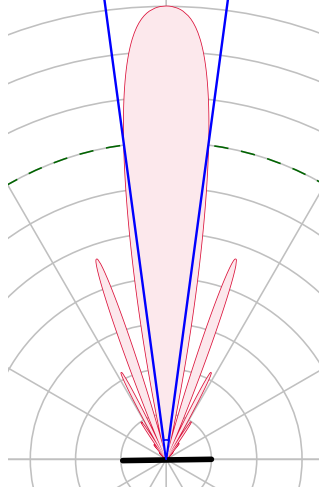


Figure 2.4: Far field beam shape and its *beamwidth* (in blue).

compute the direction of the incoming sound wave.

Another possibility is to apply signal processing by delaying the received signal from one hydrophone w.r.t. the other and adding them together. The constructive/destructive interference effectively changes the directivity of the array and, thus, can be used to find which direction gives the strongest echo. This is known as *beamforming*.

The sequence of transducers can be made into a two dimensional array (a.k.a. a grid), making it possible to detect a full 3D direction.

TVG - Time Varying Gain

As sound waves propagates, they lose intensity through spreading and absorption. Spreading loss is usually considered to be an inverse quadratic law [3], as this is the closed surface area progression for a time-like wavefront. But for cylindrical spreading it is a simple inverse law, and for perfect plane wave there is no loss.

Absorption is conditional on the water characteristics and is modeled as a slow exponential decay. Together with spreading, they are referred as Transmission Loss (TL), in decibels (dB):

$$TL = 20 \log_{10}(r) + \alpha r ,$$

where r is the wave's total traveled distance and α a water dependent parameter (with order of magnitude of $\approx 10^{-2}$ dB/m). Sonars use this equation, with a saturation around 40dB, to compensate for the echo loss [15]. And, as distance is inferred from time measurements, this compensative gain is named Time Varying Gain (TGV). CHEW and CHITRE [16] estimated TGV gain for a Tritech's Micron sonar and suggests that it agrees with the expected.

2.1.3 Available Models

Active Sonars, besides having a common working principle, present themselves in different models for different applications. DOBSON [17] summarized the most relevant ones.

Mechanically Scanning

As seen in SubSection 2.1.2, it is possible to use the beam shape as a way to reduce the number of possible incoming directions for an echo. This is the idea behind a mechanically scanning sonar, where the transducer is mechanically rotated to cover all or part of the 360°.

The angular step between different hydrophone positions is dependent on the desired resolution, smaller steps give a better resolution, but it takes longer by doing so.

1. **Profiling** - possessing a narrow conical beam shape, they are the acoustic analog of a laser scanner (although they still have a much larger aperture than a laser). Only a single echo is recorded for each angular position, either the strongest or the first to return. Typically, applied for pipeline surveillance, they can spot structural differences and objects on sea floor.
2. **Imaging** - its fan shaped narrow beam covers a wider area than the profiling type, making it very useful for navigation and obstacle avoidance on ROVs². As its beam is wide, it usually hits the surface obliquely, receiving several echos per acoustic pulse. Each echo is displayed at a distance determined by equation (2.7) and with its strength mapped to a color scale.
3. **Side Scan** (a.k.a. towfish) - Can be either mounted on each side of a boat's hull or towed behind. Usually with a beam shape similar to an imaging sonar, it can provide a sophisticated image of the sea floor.
4. **Echo-sounder** - mounted below a boat, it has a narrow pulse (as a profiling) with the single purpose of measuring the depth of water. It is typically applied to help with navigation or constructing depths charts.

Multibeam

Multibeam sonar are based on the technique of *beamforming* (described in Section 2.1.2). It has several hydrophones, rendering it able to scan an underwater region with no moving parts.

²Remotely Operated underwater Vehicle.

1. **Profiling** - similar in application to its mechanically scanning counterpart, it has multiple narrow conical beam receivers that record the signal. Instead of moving its transducer, it amplifies and processes (through *beamforming*) the received signal to identify the position of the strongest returned echo, then creating a high-speed cross-sectional profile.
2. **Imaging** - it is much quicker than a Mechanical Imaging Sonar, being very similar to a Multibeam Profiling their difference lies on beamwidth. It possesses a wide angle acoustic transmitter and multiple narrow beam receivers, applying *beamforming* to the received signal.

The array size of hydrophones is critical for enhancing resolution, longer arrays have a better angular resolution. To overcome physical limitations a technique known as *SAS* (Synthetic Aperture Sonar) may be applied. The transmission of several acoustic pulses in a line is used to emulate the presence of a longer array, by means of signal processing on the reception.

2.2 Simulation

Computational ocean acoustics explores algorithms that model the ocean as an acoustic medium. Works on this matter are well documented by ETTER [3]. Most of these works focus on very long range simulations, with its most important features been the ocean floor and sub-bottom region.

This work aims to reconstruct and simulate near-range partially closed environments, as those created by humans. The motivation for such a choice comes from the application on hydroelectric power plant water intakes, which is a corridor-like environment with possible obstacles on the bottom. This kind of environment is not well covered on the underwater acoustics literature, as such, some simulations techniques are borrowed from the closely related area of *room acoustics*.

When constructing a simulation, one has to consider the trade-off between simplicity, performance and accuracy. There are several possible techniques with different applications and assumptions, this chapter will cover the most classic ones and further explore *ray theory*, which has been used for the simulation presented here. For a more comprehensive view on this and other techniques, see LURTON [7], JENSEN *et al.* [18].

2.2.1 Techniques Overview

The idea behind sound simulation techniques is to solve the wave equation (2.2) considering all the physical interfaces as boundary conditions. The equation, how-

ever, cannot be analytically solved due to common present discontinuities caused by occlusions, specular highlights and other facts that result in large variations of field over small regions of the domain of integration [19].

The single most important reason that differentiates the several approaches described here is the *wave frequency*. For high-frequency (where sound speed do not vary much in a wavelength scale) geometric methods (ray theory) are justifiable and preferable (in the computational sense) [20]. In the case of low/mid - frequency or in the presence of caustics³, other wave methods (e.g. finite elements, normal modes, parabolic approximation) should be applied.

Instead of using the full wave equation, the methods work with a simplified time-independent version. As it is a linear equation, it can be assumed that the equation (2.2)

$$\nabla^2 p = \frac{1}{c_0^2} \frac{\partial^2}{\partial t^2} p,$$

has a solution where time dependence is an harmonic function, as the standard method for solving linear differential equations:

$$p(\mathbf{x}, t) = \text{Re}(\psi(\mathbf{x})e^{-i\omega t}), \quad (2.8)$$

where \mathbf{x} is the space coordinate while t is the time and ω interpreted as angular frequency. The exponential function considered is the complex exponential with i being the imaginary unit. The real part $\text{Re}(\bullet)$ is taken as p is real-valued, but $\psi(\mathbf{x})$ is a complex-valued function over space.

Substituting it back into (2.2), gives (dropping explicit parameters again):

$$\text{Re}(\nabla^2 \psi e^{-i\omega t}) = \text{Re}\left(-\left(\frac{\omega}{c_0}\right)^2 \psi e^{-i\omega t}\right)$$

Defining $k \equiv \frac{\omega}{c_0}$ (a.k.a. the wave number) and rearranging terms:

$$\text{Re}((\nabla^2 \psi - k^2 \psi)e^{-i\omega t}) = 0$$

As the harmonic $e^{-i\omega t}$ is equivalent to a rotation in the complex plane, the equation will be satisfied for all t if:

$$(\nabla^2 - k^2)\psi = 0 \quad (2.9)$$

Equation (2.9) is known as the (homogeneous) *Helmholtz equation* and describe the time-independent part of the wave propagation. The values of k and ω can be physically interpreted as the spatial and temporal angular frequency of the wave.

³A region of high constructive interference that geometrically gives a point of infinity rays convergence.

As the wave equation is linear, superposition applies, being reasonable to take into consideration one wave frequency at a time and superpose all these harmonics by Fourier synthesis [6].

Fourier synthesis is the calculation by *Helmholtz equation* of each independent frequency:

$$\psi_\omega(\mathbf{x}) = \int_{-\infty}^{\infty} p(\mathbf{x}, t) e^{i\omega t} dt ,$$

and reconstruct the wave equation back by:

$$p(\mathbf{x}, t) = \int_{-\infty}^{\infty} \psi_\omega(\mathbf{x}) e^{-i\omega t} d\omega .$$

These equations are the inverse and forward Fourier transform, respectively.

FEM - Finite Element Method

Finite Element Methods try to numerically find a solution to the wave equation by discretizing space, and time in some cases. It considers the equation (2.2) for inside the environment and the boundary conditions:

$$\frac{\partial}{\partial \mathbf{n}} p = -\rho_0 \frac{\partial^2 x_n}{\partial t^2} \quad \text{on the source ,}$$

$$c_0 \frac{\partial}{\partial \mathbf{n}} p = -\frac{1 - R_c}{1 + R_c} \frac{\partial}{\partial t} p \quad \text{on other interfaces ,}$$

where \mathbf{n} is the normal direction of the surface, ρ_0 is the medium density and x_n is the displacement of the acoustic membrane. The reflection coefficient R_c might depend on the interface, but as FEM are used for small frequency bands, it is a minor problem [21].

To create a linear system, the pressure function is approximated by a superposition of functions, e.g. sum of piecewise quadratic functions $p(\mathbf{x}, t) = \sum_{i=0}^N p_i(t) \varphi_i(\mathbf{x})$, applied to the wave and boundary equation and integrated w.r.t. φ_i . Giving a large set of ordinary differential equations:

$$\begin{aligned} M\ddot{p} + D\dot{p} + Kp &= Fu \\ y &= Pp \end{aligned}$$

with M, D, K being $N \times N$ matrices, p being the vector with coefficients p_i , Fu the input converted into a force and P some selection matrix to output the pressure on the desired points. This model can be written and solved as generalized state-space model:

$$\begin{aligned} E\dot{\hat{x}} &= A\hat{x} + Bu \\ y &= C\hat{x} \end{aligned}$$

$$\hat{x} = \begin{bmatrix} p \\ \dot{p} \end{bmatrix}, \quad E = \begin{bmatrix} I & 0 \\ 0 & M \end{bmatrix}, \quad A = \begin{bmatrix} 0 & I \\ -K & -D \end{bmatrix}, \quad B = \begin{bmatrix} 0 \\ F \end{bmatrix} \quad \text{and} \quad C = \begin{bmatrix} P & 0 \end{bmatrix},$$

There can be made more simplifications, but it is enough to highlight the limitations of the method (for more details, refer to DEINES *et al.* [21]). The dimension of the state is twice the number N of functions used in the approximation and that depends on the frequency:

$$N = \left(\frac{nLf}{c_0} \right)^3,$$

where L is a typical dimension in the environment, $f = \frac{\omega}{2\pi}$ the frequency and n the number of elements per wave, that should be 3 ou 4 for a good approximation [21].

Given that the size of the state increases as the cube of the frequency, the technique can only be applied to low-frequency signals, which is not applicable to high-frequency sonar as envisioned by this work.

There is also a boundary method that uses surface integral form of the wave equation, but suffers from similar restrictions. FUNKHOUSER *et al.* [19] gives a brief introduction of the subject.

Ray theory

Geometric approaches like ray theory dates back to Newton and the corpuscular theory of light. Later found to be better described as a wave, the geometric theory of light is still a very important and useful tool. The sound ray theory follows a similar path, they both apply to short-wavelength waves, but typical sound waves have mid-wavelength ($10\text{--}10^{-3}\text{m}$) while visible light has a much shorter wavelength ($\approx 10^{-6}\text{m}$).

To describe the ray from the wave theory, one starts by solving the Helmholtz equation (2.9) with a generic complex function of space through a polar decomposition [22, 23]:

$$\psi(\mathbf{x}) = \mathcal{A}(\mathbf{x})e^{i\omega\tau(\mathbf{x})}. \quad (2.10)$$

Here, $\tau(\mathbf{x})$ can be interpreted as the time it takes the sound to reach the location

\mathbf{x} and $\mathcal{A}(\mathbf{x})$ the amplitude of the signal at that point. Substituting it back to (2.9) and separating real and imaginary parts, two equations can be obtained (omitting arguments):

$$\frac{\nabla^2 \mathcal{A}}{\mathcal{A}} - (\omega \nabla \tau)^2 + k^2 = 0, \quad (2.11a)$$

$$2(\nabla \mathcal{A} \cdot \nabla \tau) + \mathcal{A} \nabla^2 \tau = 0. \quad (2.11b)$$

The geometric approximation is the assumption that the amplitude does not change much on the wavelength scale, mathematically expressed as:

$$\frac{\nabla^2 \mathcal{A}}{\mathcal{A}} \ll k^2. \quad (2.12)$$

Applying this approximation to (2.11a) and using the fact that $\omega = kc_0$:

$$\|\nabla \tau\| = \frac{1}{c_0}. \quad (2.13)$$

The equation (2.13) is known as the *Eikonal equation* and defines the surfaces of constant phase. Equation (2.11b), called the transport equation, can then be used to find the pressure amplitude of the wave. However, when considering intensity, conservation of energy can be used as will be seen later in SubSection 2.2.2.

The rays are, by definition, the perpendicular lines to the wavefronts defined by equation (2.13) which, with length parametrization, is:

$$\frac{dr}{ds} = c_0 \nabla \tau, \quad (2.14)$$

where $r(s)$ is the path follow by the ray, and s the ray length. To verify that it is a length parametrization, one has to square (2.14) and use (2.13) to find:

$$\left\| \frac{dr}{ds} \right\| = 1,$$

showing that it is a unit norm tangent vector. To find the ray path, first take the gradient of (2.13) squared:

$$\nabla(\|\nabla \tau\|^2) = \nabla \left(\frac{1}{c_0^2} \right), \quad (2.15a)$$

$$2\mathbf{H}(\tau) \nabla \tau = 2 \frac{1}{c_0} \nabla \left(\frac{1}{c_0} \right), \quad (2.15b)$$

$$c_0 \mathbf{H}(\tau) \nabla \tau = \nabla \left(\frac{1}{c_0} \right). \quad (2.15c)$$

$\mathbf{H}(\bullet)$ is the Hessian. The derivative of (2.14) (divided by c_0) w.r.t. s is:

$$\frac{d}{ds} \left(\frac{1}{c_0} \frac{dr}{ds} \right) = \frac{d}{ds} (\nabla \tau), \quad (2.16a)$$

$$\frac{d}{ds} \left(\frac{1}{c_0} \frac{dr}{ds} \right) = \mathbf{H}(\tau) \frac{dr}{ds}. \quad (2.16b)$$

Using (2.14) and (2.15c) in the r.h.s. of (2.16b):

$$\frac{d}{ds} \left(\frac{1}{c_0} \frac{dr}{ds} \right) = \mathbf{H}(\tau) (c_0 \nabla \tau), \quad (2.17a)$$

$$\frac{d}{ds} \left(\frac{1}{c_0} \frac{dr}{ds} \right) = \nabla \left(\frac{1}{c_0} \right). \quad (2.17b)$$

The equation (2.17b) can now be integrated to give the ray path. Considering the important case of constant sound velocity c_0 (as assumed elsewhere in this work):

$$\nabla \left(\frac{1}{c_0} \right) = 0.$$

So, (2.17b) (with (2.14)) can be easily solved to:

$$r(s) = r_0 + (c_0 \nabla \tau_0) s, \quad (2.18)$$

where r_0 is the ray origin, $\nabla \tau_0$ is the gradient of τ anywhere along the ray. This is the equation of a line, which show that acoustic rays travel as a straight line on constant velocity mediums for a high-frequency approximation.

Further considerations on reflection and refraction may rely on the *Snell law* similar to the electromagnetic case, because the eikonal equation is equivalent to the *Fermat's principle of least time*. If the first variation of the time functional is zero:

$$\delta T[C] = \delta \int \frac{1}{c_0(\mathbf{x})} \|\mathbf{x}'\| ds = 0.$$

Here, $\mathbf{x}(s)$ is a parametrization of the path C , $\mathbf{x}'(s)$ the tangent vector at s and the integral $T[\bullet]$ is the time to traverse C . The *Euler-Lagrange equations* give

$$\nabla \left(\frac{1}{c_0} \|\mathbf{x}'\| \right) - \frac{d}{ds} \nabla' \left(\frac{1}{c_0} \|\mathbf{x}'\| \right) = 0,$$

where ∇' is the gradient taken on the tangent space containing \mathbf{x}' , which becomes:

$$\|\mathbf{x}'\| \nabla \left(\frac{1}{c_0} \right) = \frac{d}{ds} \left(\frac{1}{c_0} \frac{\mathbf{x}'}{\|\mathbf{x}'\|} \right).$$

By considering a length parametrization r such that $\|r'\| = 1$, the result is the

same as (2.17b), so all the results follow.

It is important to highlight that this simplification relies only on the high-frequency assumption [24], given at equation (2.12). A more complete mathematical description of the physics behind ray theory can be found at FILIPPI *et al.* [6].

An important result, commonly applied on algorithms derived from ray theory, is the summation of energy/intensity of incoherent rays at a point. It starts by taking the norm of the intensity (2.4) and applying the pressure definition to it (2.8) to get⁴

$$I = g_0 \mathbb{E}[|\psi|^2], \quad (2.19)$$

where $g_0 = \frac{1}{\rho c_0}$ (the inverse of the characteristic impedance), I the intensity and ϕ the wave. For a single ray, (2.10) becomes:

$$I = g_0 \mathbb{E}[|\mathcal{A}|^2].$$

To consider the contribution of a set of incoherent rays ψ_i (i.e. uncorrelated), the total ψ becomes:

$$\psi = \sum_i \psi_i, \quad (2.20)$$

with the established fact that the expected value of a wave is zero (i.e. the mean pressure variation is zero), the condition becomes⁵:

$$\text{cov}(\psi_i, \psi_j) = \mathbb{E}[\psi_i \psi_j^*] = 0. \quad (2.21)$$

The resulting equation of the intensity (2.19) for a full wave (2.20) is:

$$\begin{aligned} I &= g_0 \mathbb{E} \left[\left| \sum_i \psi_i \right|^2 \right] = g_0 \mathbb{E} \left[\left(\sum_i \psi_i \right) \left(\sum_j \psi_j \right)^* \right] \\ &= g_0 \mathbb{E} \left[\sum_i |\psi_i|^2 + \sum_{i \neq j} \psi_i \psi_j^* \right] \\ &= g_0 \mathbb{E} \left[\sum_i |\psi_i|^2 \right] + g_0 \mathbb{E} \left[\sum_{i \neq j} \psi_i \psi_j^* \right] \\ &= g_0 \sum_i \mathbb{E} [|\psi_i|^2] + g_0 \sum_{i \neq j} \mathbb{E} [\psi_i \psi_j^*] \\ &= \sum_i g_0 \mathbb{E} [|\psi_i|^2], \end{aligned}$$

⁴Here, $\mathbb{E}[\bullet]$ means the expectation for clarity.

⁵Here, ψ_i^* is the complex conjugate of ψ_i for better reading.

Which implies:

$$I = \sum_i I_i. \quad (2.22)$$

This assumption of incoherent rays will be a common point among ray tracing algorithm, mainly because it implies the summation of ray intensities I_i to a single intensity. It is a reasonable assumption on mildly complex environments with diffuse (scattering) surfaces, which is explained by Ray Theory in SubSection 2.2.2.

Normal modes

When there is a preferred direction, or a general axis symmetric medium, like the ocean (which is generally treated as a horizontally stratified medium), a cylindrical parametrization becomes a useful coordinate system. The principal axis, in our case depth, contains the superposition of normal modes while the other dimensions carry the traveling wave.

There are slightly different mathematical approaches to Normal Modes Theory in the literature [3, 20, 22]. The following brief description rely on the techniques of ETTER [3]. Writing the solution of (2.9) as a product of a “depth” (principal axis) function $N(z)$ and a horizontal range function $H(r)$:

$$\psi = N(z)H(r),$$

leads to a separation of variables on the ODE, with k_0 as separation constant:

$$\frac{d}{dz}N + (k^2 - k_0^2)N = 0, \quad (2.23a)$$

$$\frac{d^2}{dr^2}H + \frac{1}{r}\frac{d}{dr}H + k_0^2H = 0. \quad (2.23b)$$

The normal mode equation (2.23a) describes the pressure field along the depth. Equation (2.23b), on the other hand, describes the traveling portion of the wave, that happens in the horizontal plane. The full solution for ψ is found by solving both equations. The equation (2.23a) is a classic eigenvalue problem for the differential operator, whose solutions, including boundary conditions, are known as Green’s function G [25]. The horizontal equation (2.23b) is a zero-order Bessel equation, so it may have its solution written in terms of the zero order Henkel function of the first kind ($H_0^{(1)}$)⁶. Putting these solutions together, for a monochromatic point source:

$$\psi(z, r) = \int_{-\infty}^{\infty} G(z, z_s; k_0) H_0^{(1)}(k_0 r) k_0 dk_0, \quad (2.24)$$

⁶ $H_0^{(1)}(x) = J_0(x) + iY(x)$, where J_0 and Y_0 are the zero-order Bessel functions of first and second order, respectively. More details on these functions, see ABRAMOWITZ and STEGUN [26].

where z_s is the source position on the principal axis. The evaluation of the integral as it appears is impractical, thus some simplifications are required.

The Green's function G can be expanded as a bilinear summation of orthonormal functions (u_n), the *normal modes* [27], weighted by using their respective eigenvalues (k_n), the natural frequencies. The real integral of (2.24) can be evaluated through *contour integration* to exploit the residue of the poles present on the natural frequencies. But this requires choosing a Riemann sheet for the integral and evaluate the branch line integral separately [18, 28]:

$$\psi = \oint \sum_n \frac{u_n(z) \overline{u_n(z_s)}}{k^2 - k_n^2} H_0^{(1)}(k_0 r) k_0 dk_0 + I_{\text{branch-cut}} . \quad (2.25)$$

The branch line integral $I_{\text{branch-cut}}$ can be physically interpreted as the contribution of all other modes spectrum (those that are not normal modes), representing modes that propagates through the ocean floor (being strongly attenuated) and near-field, that decays exponentially with distance. Assuming that the horizontal distance is several times the water depth, the branch line term is ignored in most theoretical developments.

Therefore, by assuming a far-field approximation ($k_0 r \ll 1$), besides disregard the branch line integral, it is possible to consider an asymptotic expansion for the Hankel function and evaluate the contour integral, obtaining [3]:

$$\psi = g(r) \sum_n \frac{u_n(z) \overline{u_n(z_s)}}{\sqrt{k_n}} e^{i(k_n r - \frac{\pi}{4}) - \delta_n r} . \quad (2.26)$$

Here, $g(r)$ is a general function of the range and δ_n the attenuation coefficient. In practice, the summation ranges over only a bounded number of modes, but this number increases with frequency, which leaves it as undesirable for high-frequency waves.

One of the advantages of normal modes over ray theory lies on the fact that, for each source/receiver position, the ray approach have to run a full simulation of the rays, while the normal modes have a closed form (like (2.26)) that easily adapts to new combinations of these parameters. In contrast, normal modes are constrained by the source frequency, in fact by the number of modes to be computed, and generally requires deeper knowledge of the environment. The attenuation coefficient (δ_n) in the ocean, for example, depends on water absorption, ocean sediment layer absorptions, compressional and shear attenuation on the basement, measures of the modes interactions with both sediment and basement (compressional and shear mechanisms) and statistics on the water-sediment boundary and sea surface as well.

Parabolic approximation

The parabolic approximation replaces the Helmholtz equation (2.9), which is an elliptic partial differential equation, by a simplified parabolic version. This approximation dates back to the middle of the XXI century, in the context of tropospheric radio wave propagation.

The normal mode solution do not handle well non-stratified mediums. To overcome this limitation parabolic approximation is constructed to handle slow varying mediums. The variation is made explicit by $k = k_0 n(r, z)$, where $n(r, z)$ is a sound refractive index [7]. The Helmholtz equation becomes:

$$(\nabla^2 - k_0^2 n^2(r, z))\psi = 0. \quad (2.27)$$

The solutions are assumed to have a fast varying horizontal field $H_0^{(1)}(k_0 r)$ and overall slow fluctuations $F(r, z)$:

$$\psi(r, z) = F(r, z)H_0^{(1)}(k_0 r).$$

Assuming asymptotic behavior to the Hankel function (similar to normal modes development) and applying it to (2.27):

$$\frac{d^2}{dr^2}F + 2ik_0 \frac{d}{dr}F + \frac{d^2}{dz^2}F + k_0^2(n^2 - 1)F = 0. \quad (2.28)$$

By the assumption that $F(r, z)$ is a slow varying field, the $\frac{d^2}{dr^2}F$ term is neglected and (2.28) gives rise to the parabolic equation. LURTON [7] proceeds further by discretizing the horizontal directions, without defining explicit dependence on the Hankel function, and using an approximation for the differentials on z through pseudo-differential operator.

The parabolic equation can then be solved numerically, but the grid size vary with frequency, becoming costly for high-frequency waves. For more details, see JENSEN *et al.* [18].

2.2.2 Ray Theory

Ray Theory provides a good way to treat high-frequency sound propagation, far from caustics, that retain an intuitive meaning. Introduced in Subsection 2.2.1, it is very similar to its electromagnetic counterpart. Each ray carries an energy density from the source that decays as it travels through the medium (Transmission loss). When it encounters an obstacle (e.g. sea floor, sea surface, man made surfaces), it (back)scatter to the source (2.11b). That is the classical (non-multipath) description [3, 7, 29, 30], summarized by a sonar equation as:

$$RL = SL - DI - TL + TS \quad (2.29)$$

Each of these acronyms corresponds to energy (intensity), or energy variation, written in decibels (2.5):

1. RL is the Received Level - $10 \log_{10}([\text{Received intensity}]/[\text{reference intensity}]^7)$
2. SL is the Source Level - $10 \log_{10}([\text{Intensity at } 1\text{m}]^8/[\text{reference intensity}])$
3. DI is the Directivity Index - $10 \log_{10}([\text{Directional loss}]^9)$
4. TL is the Transmission loss - Intensity loss through absorption and spreading while propagating (in dB).
5. TS is the Target Strength - ratio between the intensity of outgoing and incoming rays on a target hit (in dB).

Equation (2.29) does not fully describes how the simulation using ray theory should work, but gives a good insight on the elements that must be considered. SL can be inferred by the sonar power and efficiency, DI comes from the sonar beam pattern, TL is dependent on the medium, but is compensated by the sonar TVG (see subSection 2.1.2) and TS is defined by a material dependent BRDF (Bidirectional Reflectance Distribution Function), described further ahead.

Ray Interaction

For a more faithful sonar response, advanced simulation techniques based on ray theory can be applied. And, thus, requires careful consideration on the most important interactions of the rays with the interfaces, namely: **transmitted rays**, **reflected rays** and **scattered rays**, see Figure 2.7.

Transmitted Rays

When a radiant energy, in this setup represented by a ray, hits a point on a surface (or a general interface) part of the energy is absorbed, part is transmitted and, yet, another part bounces back. Transmitted rays represent the energy that goes through the interface, their intensity for each direction is mathematically defined by the BTDF (Transmitted Scatter Distribution Function) [31] (see RÖBER *et al.* [32] for an acoustic approach).

⁷Intensity of plane wave with pressure amplitude of 1 μPa .

⁸for an equivalent omnidirectional source.

⁹with respect to an omnidirectional source.

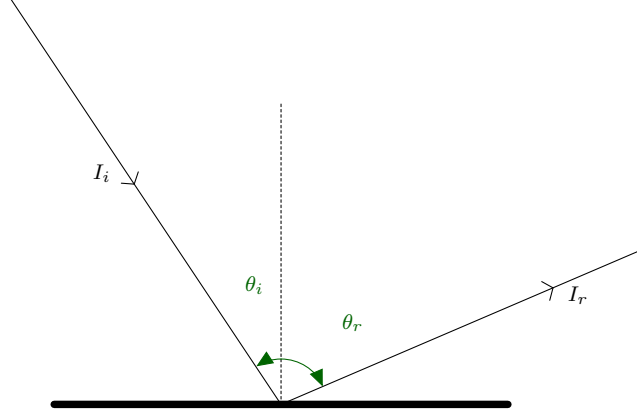


Figure 2.5: Incident and reflected rays with respective angles.

Scattered and Reflected rays

The treatment for reflected and scattered rays starts together by means of the BRDF (Bidirectional Reflectance Distribution Function) [29, 33, 34], which works similar to BTDF. On perfect smooth surfaces, its BRDF exhibits a single direction, the specular reflection, where the ray intensity is non-zero at the same plane of incident ray and the same angle with the surface normal vector. This kind of reflection is responsible for mirror like effects, e.g. sound that hits the still water surface from within [3, 7].

The other extreme case is the perfect diffuse reflection (usually called scatter in acoustics), where a rough surface reflects same perceived energy (radiance) in all directions, thus following a cosine law (Lambert's Cosine Law) with respect to the incident and reflected(scattered) angles [35, 36]:

$$I_r \propto I_i \cos(\theta_i) \cos(\theta_r), \quad (2.30)$$

where I_i , I_r and θ_i , θ_r are the intensity and angle with the surface normal for the incident and reflected rays, respectively (Figure 2.5). The proportionality constant is material dependent and should not exceed $1/\pi$, because that would violate energy conservation.

If incoming and reflected rays have the same direction, the angle is the same and the situation is called a *backscatter*:

$$I_r \propto I_i \cos^2(\theta_i).$$

There is some confusion in the literature about the cosine being or not squared [3, 7, 34, 36–38]. Possible explanations are mixing intensity information with pressure or related quantities, as intensity and radiance. This cosine law, for a single scatter,

describes the Target Strength, in dB:

$$\text{TS} = A + 20 \log_{10}(\cos(\theta_i)).$$

Here, A is the equivalent of the proportionality constant. Under the assumption of no energy loss through transmission or absorption, $A = -10 \log_{10}(\pi) \text{dB} \approx -5 \text{dB}$. More realistic values vary from -17dB for basalt ridge cliffs to -27dB for sediment pond [39]. Transmission and reflection between multiple sediment layers at the bottom of the ocean can be treated as a single entity, subbottom scattering, that introduces a delay and a displacement of the reflection [3], that case will not be covered by the simulation procedure proposed in this thesis. A remarkable property of the scattered rays is the incoherence which makes possible to add the energy (intensity) contributions for each ray directly, according to equation (2.22).

Rough ocean surface, in the presence of wind, also backscatters, but not as a perfect scatter. Its scattering properties have been modeled in a variety of ways [38], like Kirchhoff model [39]:

$$\text{TS} = -10 \Gamma^2 \log_{10}(e) \approx -4.34 \Gamma^2,$$

where $\Gamma = 2kh \cos(\theta_i)$, k is the acoustic wavenumber (2.9), h is the rms height of the surface.

A general surface does not follow neither a perfect cosine law nor is a perfect reflector, but is useful to model as a compromise of both [37, 40], even some standards for acoustic measurement (e.g. ISO) split between these two types of reflection [41]. An absorption/transmission factor α defines the fraction of the energy that does not reflect back, and a scattering factor δ the fraction of the reflected energy that is scattered (figure 2.6).

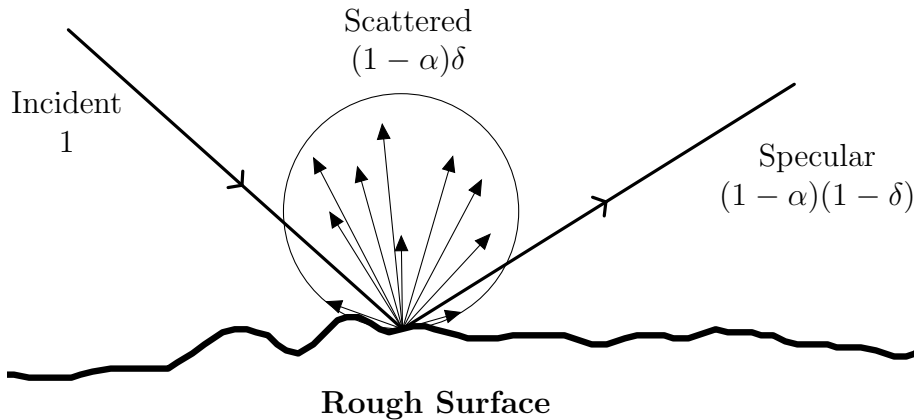


Figure 2.6: Scattering reflection weighted.

This weighting concept is explored to create a full BRDF function as $\rho(\vec{i}, \vec{r}) = (1 - \alpha)(\delta \rho_{\text{scat}}(\vec{i}, \vec{r}) + (1 - \delta) \rho_{\text{spec}}(\vec{i}, \vec{r}))$. For a numerical treatment, one option is to

discretize the solid angles as SILTANEN *et al.* [42] describes; another is to model as computer graphics, where, instead of a single direction for the specular reflection, the specular reflection is a smooth function of the reflected direction with a peak at the actual specular direction. This smooth function creates a better transition from specular to scatter reflection. A standard model is Phong reflection [43]:

$$I_r \propto I_i \cos(\theta_s)^\nu. \quad (2.31)$$

Here, θ_s is the angle between the reflected direction and the specular direction. And ν a shininess constant describing how concentrated the specular reflection is. In the limit of $\nu \rightarrow \infty$ it becomes a perfect mirror.

Ray Tracing

Ray Tracing was originally an algorithm that used ray theory (described earlier in Section 2.2.1) for computer graphics with a rationale very similar to the sonar equation (2.29). It traced a ray to every point on the scene from the source and the receiver, then computed the intensity of each color, ignoring multiple reflections.

A variety of derivations from the original algorithm have been conceived. Most of the methods applied to audio were developed for computer graphics rendering, but, considering sound waves with similar constraints to those applied to light (i.e. high frequency limit), it is reasonable to apply them to auralization (sound rendering) as well.

Among the most common techniques are **Image Source**, **Beam Tracing**, **Metropolis Transport** and **Path Tracing**. Their standard implementation assume homogeneous medium, effectively propagating rays as straight lines. An important alternative, which also overcomes sharp shadows and caustics issues, is *Gaussian Beam*, that evaluates the acoustic field at every point by adding contributions of each ray. The name comes from the fact that weight of a ray decays in the paraxial direction as a gaussian. It is typically computationally more costly than other ray tracing, but has applications for inhomogeneous open environments as described by TRACER *et al.* [44].

Image Source

This method focuses on environments composed by segments on the 2D case or polygonal slices of planes on the 3D case. It works best on box-like environments, for this creates a perfect tiling of space [19] (see Figure 2.9).

For each reflective surface, a virtual source is created on the reflected position of the source, these are the primary virtual sources. A virtual source will act just like a source, although its intensity is lessened by the absorption factor of the wall. When

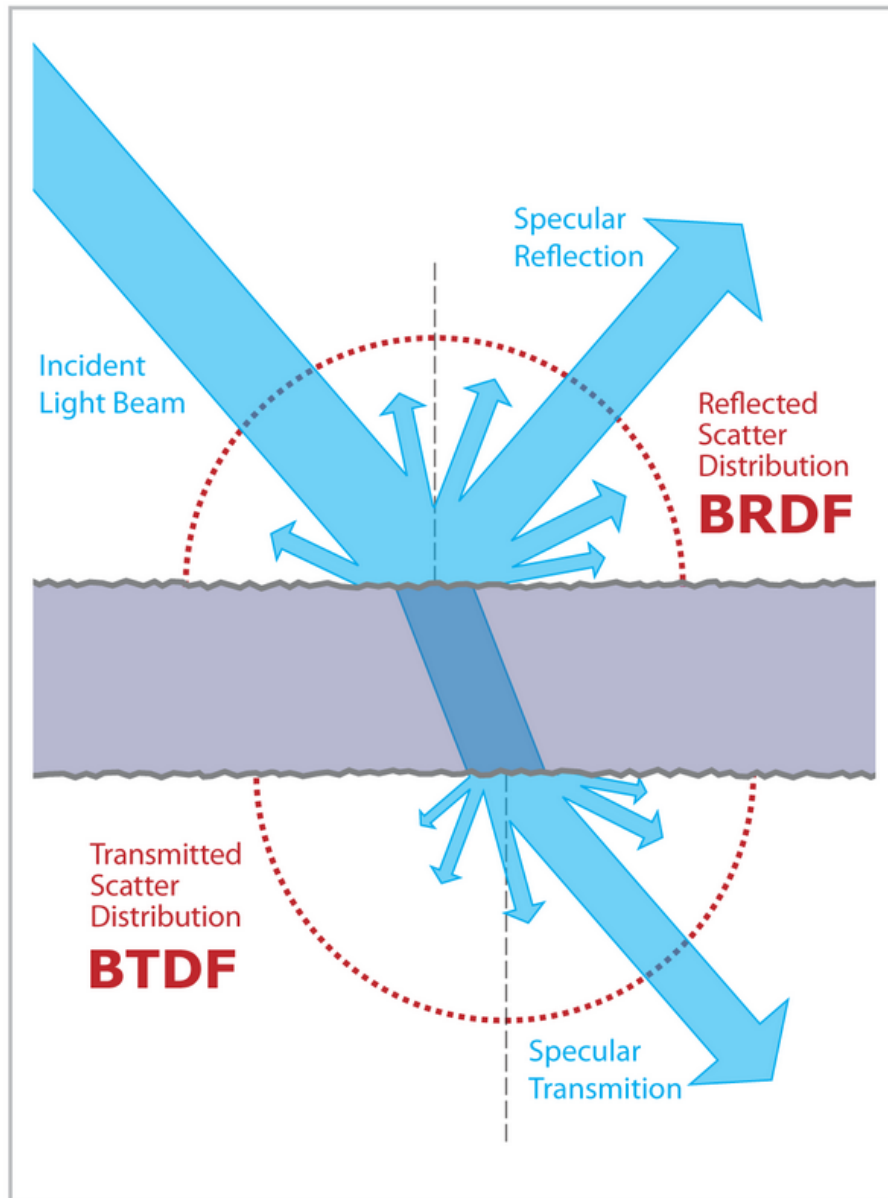


Figure 2.7: BRDF and BTDF for transmitted, reflected and scattered rays.
 (©User:Jurohi / Wikimedia Commons / CC-BY-SA-3.0)

computing the sound at point, the contribution of each source (including virtual ones) are added together, the reflections are automatically taken into account by the virtual sources.

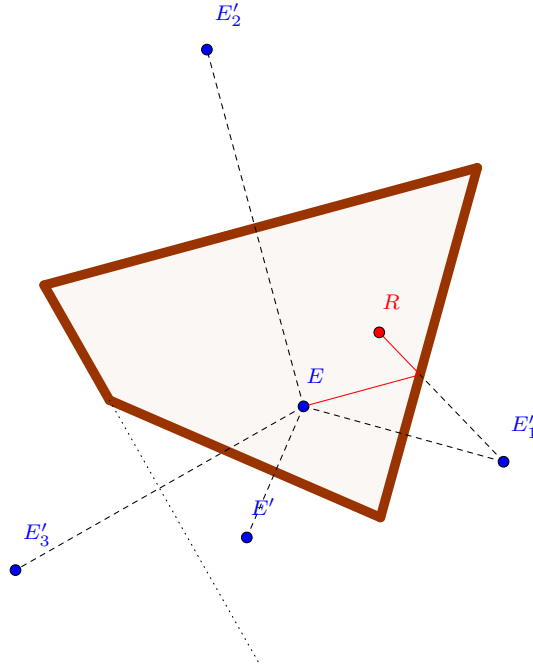


Figure 2.8: The source E and the virtual sources E', E'_1, E'_2, E'_3 . In this case, E'_3 is not a visible virtual source.

The procedure of creating the virtual sources may be repeated many times for each new virtual sources, thus more reflection are effectively calculated. The visibility of a virtual source must be validated before adding its contribution.

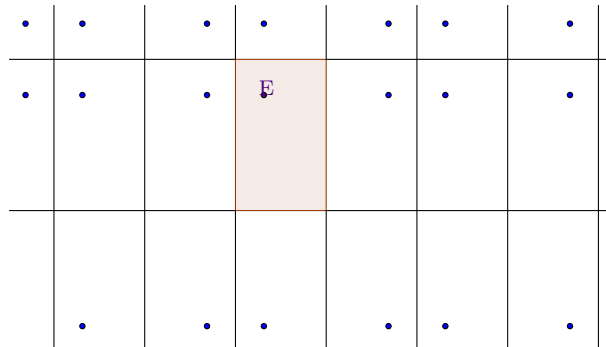


Figure 2.9: Source on a perfect tiling. The simple pattern facilitates computation.

The method does not direct implement the idea of sound scattering, but there are some possible extensions [45]. In practice, for more complex environments, only a few early reflection are generated. The number $O(n^r)$ of sources, where n is the number of surface planes and r the number of reflections, that must be created and validated grows exponentially fast.

Beam Tracing

Beam Tracing uses pyramidal beams, a collection of rays, instead of single infinitesimal rays to calculate reflections [19]. The solid angle on the source that describes available sound directions can be subdivided in pyramidal beams without overlap, avoiding sampling issues. These pyramidal beams exploit the spacial relation between nearby rays, being able to consider the propagation path without skipping any ray.

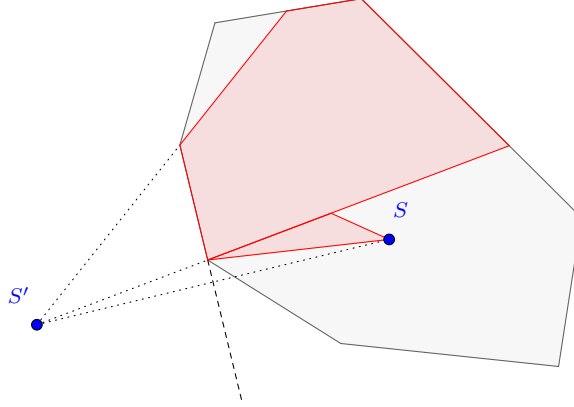


Figure 2.10: A 2D view of a pyramidal beam tracing.

The algorithm starts by subdividing the source sound directions into pyramidal regions. For each pyramidal beam, intersections with environment walls are calculated from the first encounter to the last, clipping the beam so no shadowed regions are considered. The resulting polygons of each intersection act as a new virtual source, constructed by mirroring the source as in the Image Source method. Beam Tracing, then, progresses by repeating this procedure on each virtual source, until the desired precision (number of reflections) is achieved.

It does not suffer from visibility computation issues as Image Source, but is less efficient for highly structured box-like environments. Despite working well on simple scenes (with or without occlusions), it still not handling well curved surfaces.

Path Tracing

Path Tracing is a recursive solution to the wave equation simplification used in ray theory. That can be written, in terms of the radiance ℓ (the ray energy - acoustic energy per unit of surface area per unit of solid angle), as an integral equation, the *room acoustics rendering equation* [42]:

$$\ell(\mathbf{p}, \Omega) = \ell_0(\mathbf{p}, \Omega) + \int_{\mathcal{G}} R(\mathbf{x}, \mathbf{p}, \Omega) \ell(\mathbf{x}, \vec{\mathbf{x}\mathbf{p}}) d\mu(\mathbf{x}), \quad (2.32)$$

where \mathcal{G} is the two dimensional subset of \mathbb{R}^3 comprising all surfaces, \mathbf{p} is a point over a surface, $d\mu(\mathbf{x})$ is the surface area differential at point \mathbf{x} , Ω is the outgoing energy direction, ℓ_0 the intrinsic surface radiance (in case the surface is an emitter), $\vec{\mathbf{x}\mathbf{p}}$ the unit vector in the direction to \mathbf{p} from point \mathbf{x} . The function $R(\bullet, \bullet, \bullet)$ is the *reflection kernel*, an enhanced version of a BDRF. For a non-obstructed path between \mathbf{p} and \mathbf{x} :

$$R(\mathbf{x}, \mathbf{p}, \Omega) = \alpha(\|\mathbf{p} - \mathbf{x}\|) \rho_{\mathbf{p}}(\vec{\mathbf{x}\mathbf{p}}, \Omega) \cos(\theta_i) \cos(\theta_r). \quad (2.33)$$

When there is no visibility from \mathbf{x} to \mathbf{p} , $R(\mathbf{p}, \mathbf{x}, \Omega) = 0$. Here, $\rho_{\mathbf{p}}(\vec{\mathbf{x}\mathbf{p}}, \Omega)$ is the BDRF at the point \mathbf{p} with incoming direction $\vec{\mathbf{x}\mathbf{p}}$ and outgoing energy direction Ω , θ_i and θ_r are the incoming and reflected angles with surface's normal at point \mathbf{p} for directions $\vec{\mathbf{x}\mathbf{p}}$ and Ω , respectively. Factor $\alpha(\|\mathbf{p} - \mathbf{x}\|)$ is the decay dependent on the distance $\|\mathbf{p} - \mathbf{x}\|$ caused by spreading and absorption, usually an inverse squared times an exponential factor (commented in SubSection 2.1.2).

The solution to equation (2.32) is a Neumann series:

$$\ell_{n+1}(\mathbf{p}, \Omega) = \int_{\mathcal{G}} R(\mathbf{x}, \mathbf{p}, \Omega) \ell_n(\mathbf{x}, \vec{\mathbf{x}\mathbf{p}}) d\mu(\mathbf{x}), \quad (2.34a)$$

$$\ell(\mathbf{p}, \Omega) = \sum_{n=0}^{\infty} \ell_n(\mathbf{p}, \Omega). \quad (2.34b)$$

For the actual computation, the summation on equation (2.34b) is truncated at some reasonable value of n , which is the number of reflections being considered, and the integral on equation (2.34a) can be approximated using, for example, a Monte Carlo method applying importance sampling w.r.t. the function $R(\bullet, \bullet, \bullet)$ (MUNJAL *et al.* [46] describe briefly such an algorithm). When scattering is not strong enough, it is a common practice to consider only specular directions.

Besides the success of computer graphics using the same technique, in the end of the last century there were still some concerns regarding the theoretical validity, mainly because it was shown to be uncomputable [47]. That is, it was impossible to say if a ray would ever reach a certain point. Later, this decade, it was shown by BLAKEY [48] that, if one considers computational finite precision, it can be proven to be computable.

In the case of sonar, the only important point to measure the sound intensity is on the sonar itself. A simplified approach for the integral on equation (2.34a) is to consider only the specular direction (where it is supposed to have greater radiance) and the scattered direction into the sonar, assuming the other scattered directions will die out without much affecting the sonar response.

Metropolis Transport

Metropolis Light Transport (MLT) is an incremental development over Path Tracing. It records the path taken by a ray as a tree where each reflection point is a node. By adding, removing or changing nodes, it is able to better explore the space without ruling out the work done to produce a path from source to detector.

The name comes from the use of Metropolis sampling method to explore the space, which degenerate paths that are small variations of the original one. A change in the path may be accepted or rejected (as in the original Metropolis method) and the decision strategy ensures an ergodic, unbiased and generally applicable result.

At the cost of added complexity, MLT gives better results specially around caustics and difficult to reach regions (e.g. through a narrow aperture) without degrading performance. The original paper by VEACH and GUIBAS [49] explains with great clarity the math behind as well as the results and interpretations.

2.3 Environment

Extensive literature have been written on ocean environment, from modeling its behavior to measuring its properties. Different simulation techniques have also been explored [3]. The modeling presented here, although simple, completely suits the needs of a ray tracing technique, presented in Section 2.2.2.

2.3.1 Modeling

Borrowed from computer graphics, the modeling properties of a scene objects are the same for light and sound (given the high frequency limit for which ray theory is applicable). Two distinct factors are modeled, one is geometric, which defines the shape of the object, the other is acoustic, expressing how does it interact with sound.

For the geometric part, two basic functions have to be provided: **intersection** and **normal**. **Intersection** takes a ray, defined by an origin point and a direction, and outputs the distance to the first intersection point with the object. If no intersection point is found, the distance is defined to be infinity. **Normal** receives a point on the surface of the object and return the normal vector at such a point. Algorithm 1 exemplifies the **intersection** for a rectangle, the ray's origin **O** and direction **D** are matrix with the concatenated information of all those whose intersection ought to be calculated.

Any surface can be approximated by triangulation and have these functions standardized, but it is easy to directly define for some geometric primitives. Plane, rectangle, sphere and cylinder were developed for this work.

Algorithm 1 Intersection for Rectangle

```

function INTERSECTION(O, D)                                ▷ O is ray origin, D is direction
   $\Delta \leftarrow center - \mathbf{O}$                                 ▷ center is the rectangle center
   $n \leftarrow \vec{s_1} \times \vec{s_1} / \|\vec{s_1} \times \vec{s_1}\|$           ▷  $\vec{s_1}$  and  $\vec{s_1}$  are the rectangle's half-sides
   $T \leftarrow [\vec{s_0} \ \vec{s_1}]^\dagger$                                 ▷  $\dagger$  is pseudoinverse
   $d \leftarrow \Delta \cdot n / \mathbf{D} \cdot n$                         ▷ distance to intersection point
   $P \leftarrow \mathbf{D}d - \Delta$                                 ▷  $P$  are the intersection with the rectangle's plane
   $R \leftarrow T \cdot P$                                 ▷  $R$  are the intersection described on  $[\vec{s_0} \ \vec{s_1}]$  basis
  for all  $i \in [0, \dots, \text{size}(d)]$  do
    if  $d_i < 0$  or  $|R_{i,0}| > 1$  or  $|R_{i,1}| > 1$  then
       $d_i \leftarrow \infty$                                 ▷ Check ray direction and if hit within rectangle
    end if
  end for
  return  $d$ 
end function

```

Two environments were constructed using these four geometric primitives. One box-like for the reconstruction part of this thesis, which is simple enough to study the properties of the mapping. Another, more complex and inspired by a water entrance of a hydroelectric power plant, that exhibits a richer sonar response with sound multipath and directional gain playing a more important role.

Box-like Environment

For the **box-like structure**, five planes were used thus determining a semi-infinite box with 8 meters width, 10 meters length and the bottom 3 meters from the origin. All planes are defined by a point and its normal vector.

Plane n ^o	Point	Normal Vector
0	(0, 4, 0)	(0, -1, 0)
1	(0, -4, 0)	(0, 1, 0)
2	(5, 0, 0)	(-1, 0, 0)
3	(-5, 0, 0)	(1, 0, 0)
4	(0, 0, -3)	(0, 0, 1)

Table 2.1: Five planes defining box-like environment walls.

Complex Environment

The more **complex scene** is composed of 5 rectangles, 2 planes and a sphere representing, respectively, 5 concrete walls, river floor and still surface water and a half-spherical mountain of sediments. Rectangles are defined by a central point and two perpendicular vectors, the half sides, and spheres by a center and radius.

2.3.2 Characterization

Instead of defining a full BRDF (explained in Section 2.2.2), three parameters are considered: **diffusion coefficient**, **specular coefficient** and **shininess**. All three parameters may change at every point on the surface of an object, thus defining a texture, but for the sake of simplicity only constant values over the surface were considered.

The **diffusion coefficient** and **specular coefficient** are, respectively, fractions of incident energy over a surface patch that reflects diffusely (as a lambertian reflector) and specularly. Reflections near specularly are weighed as Phong reflection for a less unrealiscaly abrupt change in reflection intensity. The **shininess** is the Phong parameter. These concepts are described in Section 2.2.2.

The actual values used came from a collection of sources in addition to experimentation and tacit knowledge (from previous sonar use), as these are difficult information to find in the literature.

For concrete, CHAUDHARI [10] studies the **reflection coefficient**, sum of **diffusion coefficient** and **specular coefficient**, to characterize the concrete’s quality following earlier measurements of LESLIE and CHEESMAN [50]. The table provided on the article (Table ??) can be used in the other direction, to simulate such a concrete quality. The individual values of **diffusion coefficient** and **specular coefficient** still have to be determined and come from an educated guess based on considerations on smoothness by ETTER [3], which claims that most of the energy goes as specular reflection for smooth surfaces. For simulation purposes it has been assumed values between 80% to 95% of the reflected energy to be specular.

Quality Of Concrete	Reflection Coefficient
Very good	0.76 or above
Good	0.69-0.74
Questionable	0.62-0.69
Poor	0.48-0.62
Very Poor	0.48 or less

Table 2.2: Quality of Concrete and Reflection Coefficient. (CHAUDHARI [10], LESLIE and CHEESMAN [50])

ETTER [3], also, provides equations relating wind speed with water surface reflection coefficient, which varies according to its roughness caused by the wind. For calm waters, there is almost no transmitted energy and all reflected energy is specular. For other materials, estimated values come from models as the one provided by MILLER [29] on Figure 2.11.

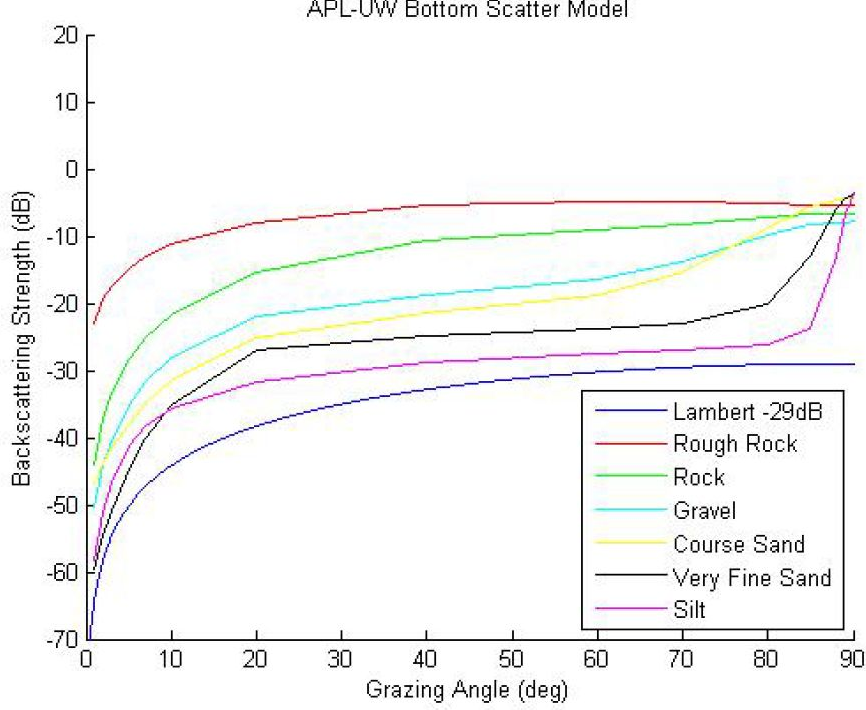


Figure 2.11: Materials reflective characteristics from MILLER [29].

2.4 Implementation

2.4.1 Algorithm

The simulation follows the ray tracing technique outlined by BELL and LINNETT [51] for side scan sonar, but applies it to a forward looking sonar imaging sonar (Section 2.1.3). It also uses a noising adding step as suggested by COIRAS *et al.* [52] with statistics provided by MAUSSANG *et al.* [53]. No movement induced distortion was considered, some approaches to add this feature is available in BELL *et al.* [54], BORAWSKI and FORCZMAŃSKI [55]. Also, spreading and absorption losses are ignored, assuming they are compensated by TVG (see Section 2.1.2).

Sonar parameters follow a Tritech's Micron sonar [56] information as output power, dynamic gain, beam step and sensibility were found on official Tritech's documentation [56, 57]. The directional gain was measured by the National Physical Laboratory, UK.

Simulation's output is, just as on the sonar, a sequence of arrays with values between 0 and 255. Each element of the sequence is a bearing, direction of the emitted sound pulse, and the array's components are the bins' values, sound intensity received at some range of distances (calculated from echo delay).

The algorithm implementation uses the programming language Python with the mathematical library NumPy, specially for efficient linear algebra. Most of the treatment uses linear algebra to treat batch of rays at once.

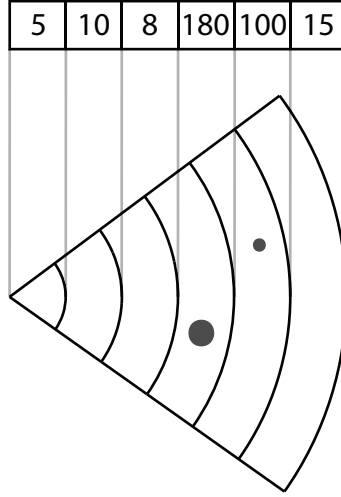


Figure 2.12: Example of an array for a bearing direction. Actual arrays are longer, depending on resolution.

Flowchart of Figure 2.13 describes the simulator logic. It starts by computing ray directions spread over a sphere centered at the sonar with uniform density, otherwise it would bias the ray trace. Not all directions are actually computed because some directions have very low gain, so rays in these directions have almost no energy, they can be discarded. To compute such a uniformly distributed directions apply transformation described by algorithm 2 for $[-\alpha, \alpha]$ and $[-\beta, \beta]$ the vertical and horizontal angular span, respectively, and N the desired number of rays. Results in Section 2.4.2 use $\alpha = 30^\circ$ and $\beta = 3^\circ$, approximately the values for which Micron cannot detect the echo.

Algorithm 2 Rays Uniform Direction

procedure UNIFORM DIRECTION(α, β, N)

$d\theta \leftarrow 2 \cos(\pi/2 - \alpha)$

$d\phi \leftarrow 2\beta$

$\rho \leftarrow \sqrt{\frac{N}{d\phi \cdot d\theta}}$

▷ Estimated density

$N_\theta \leftarrow \lceil \rho \cdot d\theta \rceil$

$N_\phi \leftarrow \lceil \rho \cdot d\phi \rceil$

▷ $U(\mathbf{x})$ generates \mathbf{x} uniform samples over $[0, 1]$

$\theta \leftarrow \arccos(d\theta \cdot (2U(N_\theta) - 1))$

$\phi \leftarrow d\phi \cdot (2U(N_\phi) - 1)$

for all $(\theta_i, \phi_i) \in \theta \times \phi$ **do**

$x_i \leftarrow \sin(\theta_i) \cos(\phi_i)$

$y_i \leftarrow \sin(\theta_i) \sin(\phi_i)$

$z_i \leftarrow \cos(\theta_i)$

$v_i \leftarrow (x_i, y_i, z_i)$

end for

return v

end procedure

The sonar bearing pace is adjustable and, following Tritech's Micron configura-

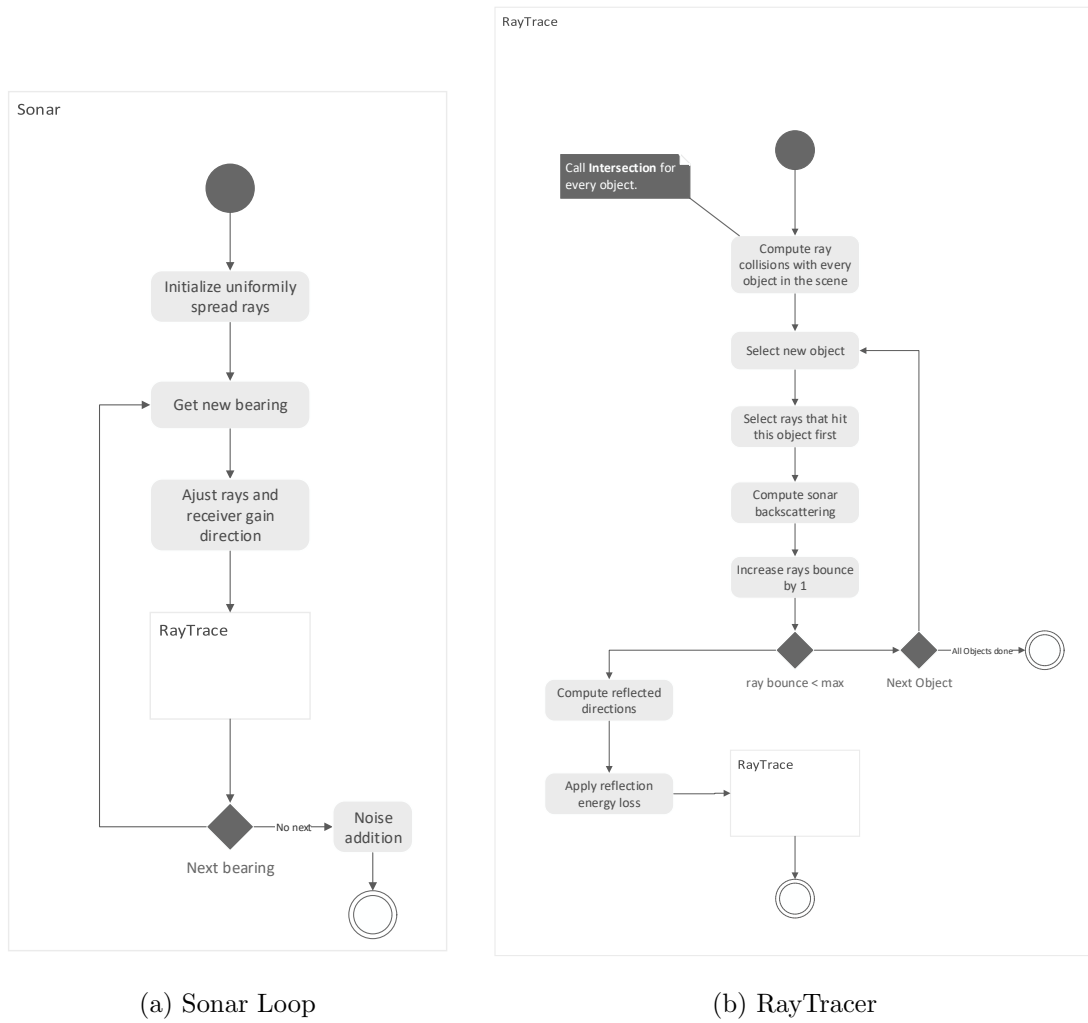


Figure 2.13: Overview of the simulation algorithm.

tion, it was set to 1.8° , thus, doing a complete scan on 200 steps. For each step, ray directions are changed (by a rotation) to match new bearing. Received gain is calculated w.r.t. the front direction (bearing), as the bearing changes the gain is automatically updated. Rays always carry 2 information: its actual intensity (disregarding distance traveled decay) and its total traveled length. A new bearing position invoke ray tracer algorithm. It begins by calling the **intersection** function (described in Section 2.3.1) for each object in the scene, passing all rays as argument. Then it loops again on every object, but now only focus on the rays that have the object as first hit, and compute the backscattering to the sonar. Backscattering strength calculation use Lambert and Phong scatterings as described in Section 2.2.2 and material parameters listed in Section 2.3.2. This strength is added to a bin (see Figure 2.12) whose position is calculated as half the full distance traveled by the ray (including previous reflections) plus a small gaussian noise. It proceeds to calculate reflection if the number of computed reflection for the ray does not exceed a maxi-

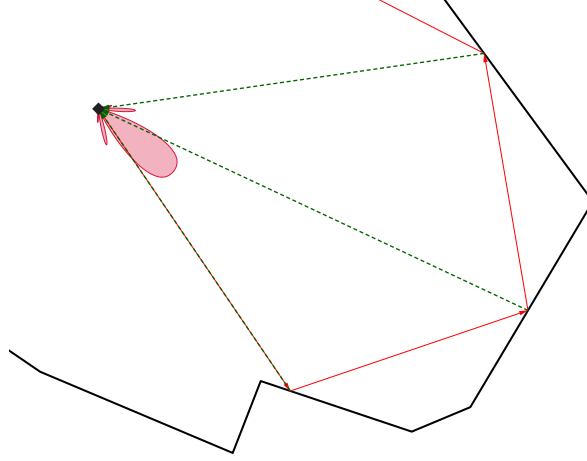


Figure 2.14: Ray Tracing: Red lines are specular reflections, green lines are diffuse backscattering.

mum value (set to 5). Reflections are simple linear transformations that depends on the surface's normal, obtained via **normal** function (Section 2.3.1). The algorithm, then, calls itself for the reflected rays, recursively.

After the whole scan is computed, bin values are normalized to $[0, \dots, 255]$ (again according to Tritech's Micron configuration). Upon these values, an additional Weibull's distributed noise is applied [53].

2.4.2 Results

For both environments described in Section 2.3.1, several sonar positions were simulated. The absolute position and orientation were chosen, but the bearing w.r.t. the environment was a random value.

Polar plots displayed here is the expected visualization, without noise filtering, when the sonar uses 500 bins of resolution with a 12 meters range. Each polar pixel has a 3° arc length, but, as the bearing step is 1.8° , they overlap while being rendered.

Box-like Environment

The half-infinity box-like structure is depicted on figure 2.15. Axis aligned sonar orientation on figures 2.15c and 2.15d make clear its rectangular cross section, while its half-infinity characteristic is visible on perpendicular oriented scans, figures 2.15a and 2.15b.

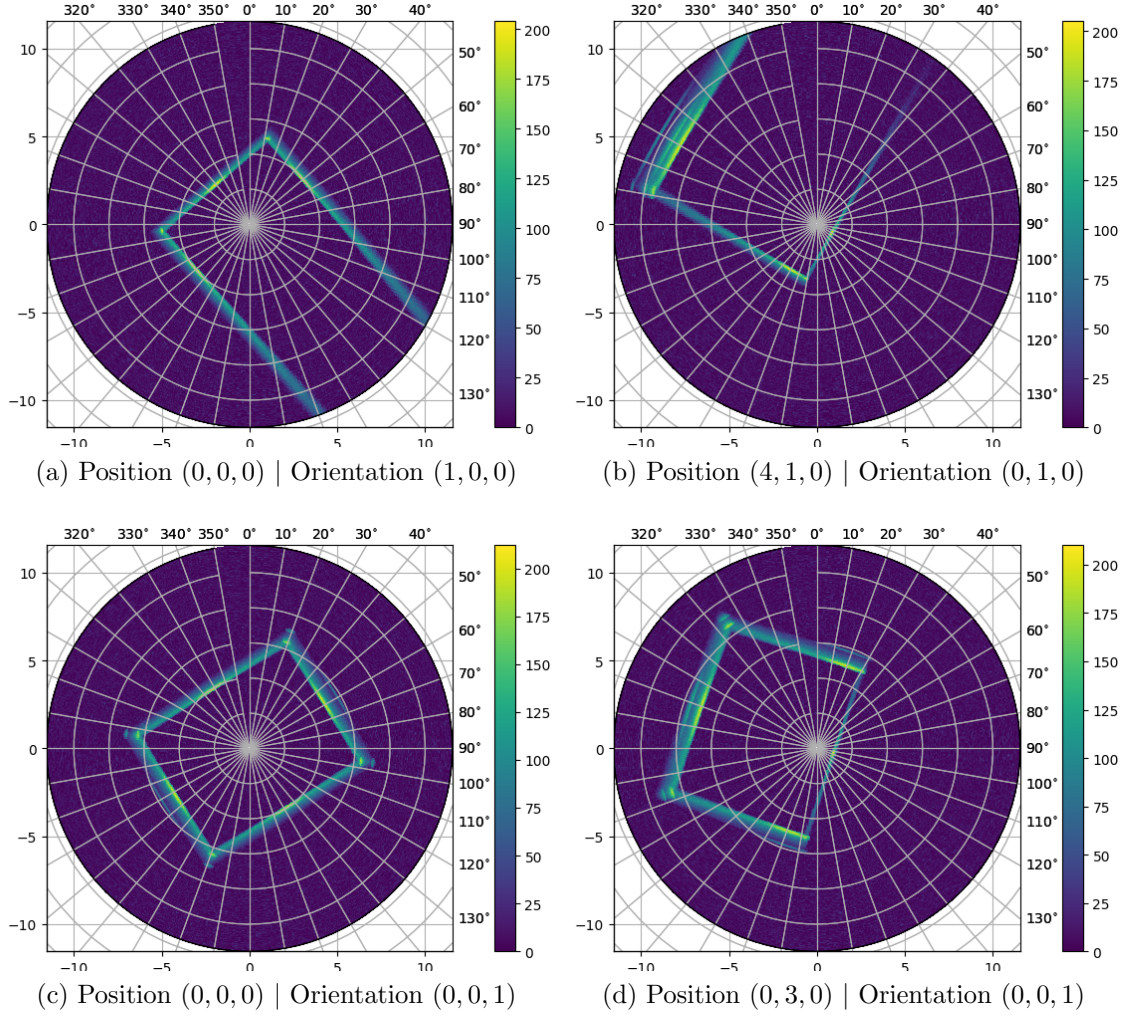


Figure 2.15: Sonar simulation for the box-like scene.

Complex Environment

Figure 2.16 shows the more complex structure from four view points. Images 2.16a and 2.16b are scans from between walls of the indent. Figure 2.16d is cross sectional view of the indent and figure 2.16c is a scan from the same position, but with different orientation, making the hemisphere at the bottom more noticeable.

Both environments reveal interesting features of a sonar scan, but they tend to be more pronounced on the complex environment. Figures 2.16b, 2.16d and 2.15b present clear signal of multipath. Another interesting feature is the halo on the background of figures 2.16a and 2.16b caused by a trade-off between the sonar directional gain and the low backscattering at shallow angles.

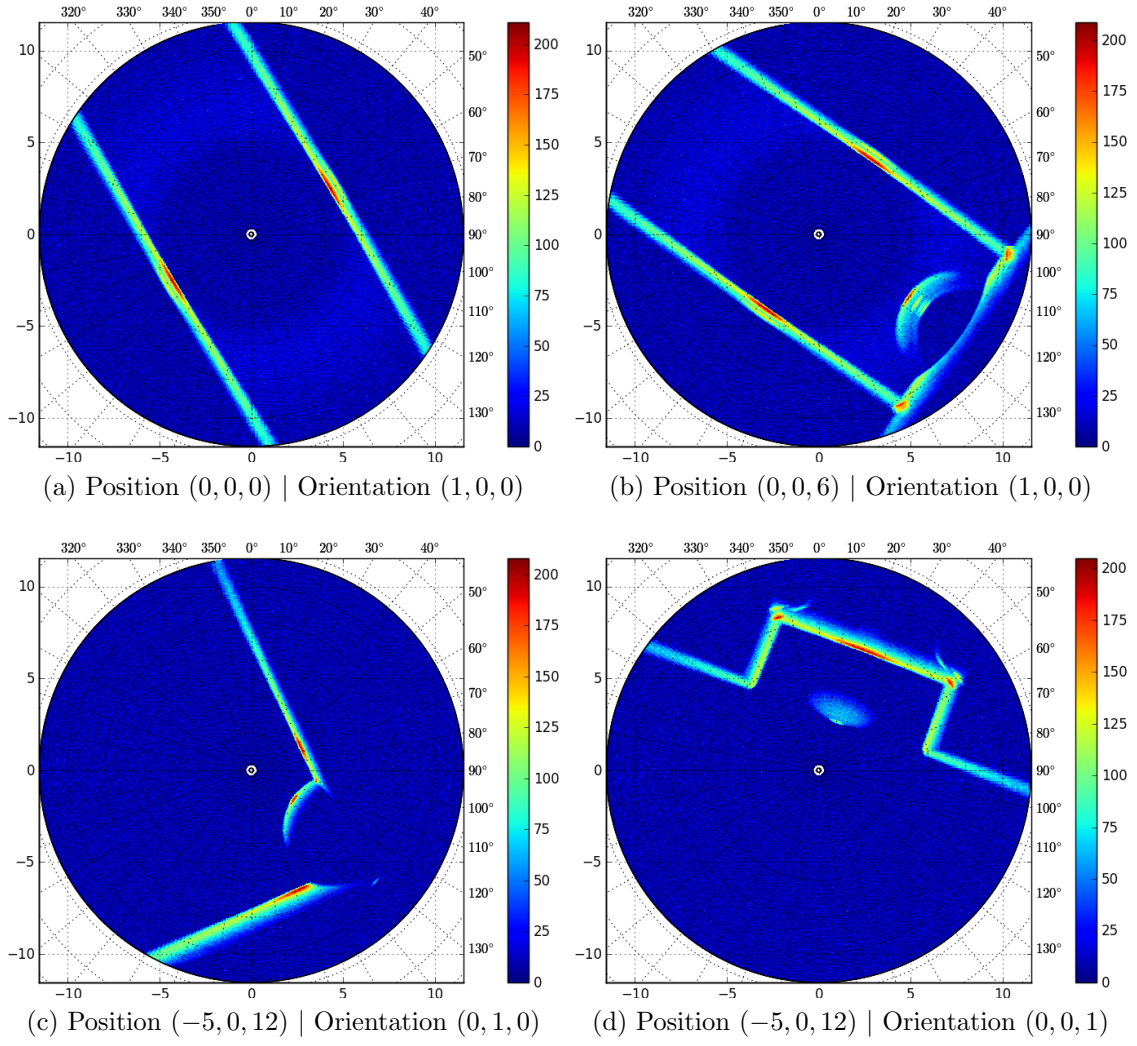


Figure 2.16: Sonar simulation for the complex scene.

Chapter 3

Mathematical Preliminaries

”Obvious” is the most dangerous word in mathematics.

Eric Temple Bell, 1938

Some more advanced mathematical tools¹ used on the development of this thesis are presented here. Other knowledge, as basic linear algebra, statistics and analysis, are taken as granted.

3.1 Hilbert Space

A Hilbert Space is a complete inner product space [58]. It is a complete metric space with respect to the metric induced by its inner product (which in turn can be thought indirectly by its induced norm). A nice picture is as a generalization of the Euclidean space. Which means intuition works well, in contrast with the broader concept of Banach Spaces, a complete normed space, where the infinite dimensional case can be quite different from what one would expect².

An inner product space [59] is a (possibly infinite dimensional) vector space V over \mathbb{C} (or \mathbb{R} by restriction), together with a map (called the **inner product**):

$$\langle \cdot, \cdot \rangle_V : V \times V \rightarrow \mathbb{C}$$

Satisfying the following properties, for all $x, y, z \in V$ and all $\mu, \lambda \in \mathbb{C}$:

I $\langle x, \lambda y + \mu z \rangle_V = \lambda \langle x, y \rangle_V + \mu \langle x, z \rangle_V$ (linear in the second argument)

II $\langle x, y \rangle_V = \overline{\langle y, x \rangle_V}$ (Hermitian symmetric)

¹As judged by the autor from the perspective of a graduated student.

²Banach Space are complete metric spaces where the metric does not come necessarily from an inner product. (See HUNTER and NACHTERGAELE [59])

III $\langle x, x \rangle_V \geq 0$ and $\langle x, x \rangle_V = 0 \Leftrightarrow x = 0$ (positive definite)

A classical example of an inner product is the Euclidean dot product.

Another important example is the inner product defined on the space $C[a, b]$ of complex (or real) valued continuous functions on the interval $[a, b]$, defined, for every f and g in $C[a, b]$ as:

$$\langle f, g \rangle_{C[a, b]} = \int_a^b f(x) \overline{g(x)} dx. \quad (3.1)$$

On any Hilbert Space \mathcal{H} the norm induced by the inner product is:

$$\|x\|_{\mathcal{H}} = \sqrt{\langle x, x \rangle_{\mathcal{H}}}, \quad (3.2)$$

where $x \in \mathcal{H}$. And the subsequent metric is defined as:

$$d_{\mathcal{H}}(x, y) = \|x - y\|_{\mathcal{H}}, \quad (3.3)$$

for any $x, y \in \mathcal{H}$.

A vector space endowed with an inner product is a *inner product space* (a.k.a. pre-Hilbert space). For it to be a Hilbert Space it also has to be complete with respect to the above metric. Completeness means that any Cauchy sequence converges in this space (which provides a suitable framework to apply the tools of calculus). A Cauchy sequence is a sequence where every term becomes arbitrarily close to each other as the sequence progress (not only to term right next to it). It can be formalized as the sequence x_1, x_2, x_3, \dots on a metric space (with a metric $d(\cdot, \cdot)$) where:

$$\forall \epsilon \in \mathbb{R}^+, \exists N \in \mathbb{Z}^+, \forall n, m > N \implies d(x_n, x_m) < \epsilon.$$

On a pre-Hilbert space, the metric is given by equation 3.3. If a metric space M is complete, then every Cauchy sequence (x_1, x_2, x_3, \dots) converges in that space, that is:

$$\exists x \in M, \forall \epsilon \in \mathbb{R}^+, \exists N \in \mathbb{Z}^+, \forall n > N \implies d(x_n, x) < \epsilon,$$

which is equivalent to write:

$$x = \lim_{n \rightarrow \infty} x_n.$$

A complete metric space can be obtained from a pre-Hilbert space, by completion, in the same way that \mathbb{Q} is “completed” to make \mathbb{R} . Although completeness is a technicality, it is easy to find examples of pre-Hilbert spaces that lacks this property. The space of continuous functions $C[a, b]$ with the inner product defined on 3.1 gives an example of pre-Hilbert space that is not complete. For it to be a Hilbert space, the space have to be extend to include some discontinuous functions, as in the larger

set of Lebesgue measurable³ functions that are square integrable (with the Lebesgue integral).

Some examples of Hilbert space are:

- Any finite dimensional vector space over the field \mathbb{R} or \mathbb{C} with the standard dot product.
- The space ℓ^2 of square-summable sequences of complex numbers, i.e. (c_1, c_2, c_3, \dots) with $c_i \in \mathbb{C}$ and $\sum_{i=1}^{\infty} |c_i|^2 < \infty$, is a Hilbert space with the inner product defined as: Given two sequences $x = (x_1, x_2, x_3, \dots)$ and $y = (y_1, y_2, y_3, \dots)$, define $\langle x, y \rangle_{\ell^2} = \sum_{i=1}^{\infty} x_i \bar{y}_i$.
- Fourier series can be seen as the representation of a square-integrable function on the interval $[0, 1]$ (member of $L^2[0, 1]$) on the orthogonal basis $\{e^{2\pi i n \theta} : n \in \mathbb{Z}\}$ with the inner product given by 3.1.

3.2 RKHS - Reproducing Kernel Hilbert Space

3.2.1 The Evaluation Functional

A *Reproducing Kernel Hilbert Space*, RKHS for short, is a special kind of Hilbert Space of functions. In a RKHS, closeness in the sense of the metric is actual pointwise proximity. That is to say, if two real-valued functions f and g on a (non-empty) set \mathcal{X} belong to a RKHS \mathcal{H} ($f, g \in \mathcal{H} \subset \mathbb{R}^{\mathcal{X}}$), then whenever $\|f - g\|_{\mathcal{H}}$ is small so is $|f(x) - g(x)|$ for all $x \in \mathcal{X}$ [60].

A more formal and useful characterization of a RKHS is consequence of studying linear operators on Hilbert Spaces. The evaluation functional $\delta_x : \mathcal{H} \rightarrow \mathbb{R}$, $\delta_x : f \rightarrow f(x)$ is easily seen as such: given $f, g \in \mathcal{H}$ and $a, b \in \mathbb{R}$, $\delta_x(af + bg) = (af + bg)(x) = af(x) + bg(x) = a\delta_x(f) + b\delta_x(g)$. When the evaluation functional is continuous on \mathcal{H} , \mathcal{H} is said to be a RKHS.

Although $L^2[a, b]$ is not a RKHS (it is not even a proper space of functions, but instead a space of classes of equivalences of functions), its bandlimited ($L^2 \cap L^1$) version $PW_{\pi} := \{f \in L^2(\mathbb{R}) \mid \text{supp } \mathcal{F}(f) \subseteq [-\pi, \pi]\}$, for example, has a continuous evaluation functional. Here, $\mathcal{F} : L^2(\mathbb{R}) \rightarrow L^2[-\pi, \pi]$ is the fourier transform [61]:

$$\mathcal{F}(f) = \frac{1}{\sqrt{2\pi}} \int f(t) e^{-i\omega t} dt \quad f \in L^2(\mathbb{R}), \quad (3.4a)$$

³The Lebesgue measurability of a, bounded with compact support, function is a highly technical exigence and the existence of a bounded non-Lebesgue measurable set (which allow the construction of such a function) is dependent on the axiomatic choice of the underlying set theory - it can only be proven with the addition of the *choice axiom* to the ZF (Zermelo-Fraenkel) set of axioms (ZFC).

$$\mathcal{F}^{-1}(\hat{f}) = \frac{1}{\sqrt{2\pi}} \int_{-\pi}^{\pi} \hat{f}(\omega) e^{i\omega t} d\omega \quad \hat{f} \in L^2[-\pi, \pi]. \quad (3.4b)$$

The proof of continuity for the evaluation functional on PW_π relies on the inverse Fourier transform (3.4b), Cauchy-Schwarz's and Parseval's theorems, used on equations (3.5c), (3.5d) and (3.5e) respectively. For $f, g \in PW_\pi$ it goes as follows:

$$|\delta_x f - \delta_x g| = |f(x) - g(x)| \quad (3.5a)$$

$$= |\mathcal{F}^{-1}(\mathcal{F}(f - g))| \quad (3.5b)$$

$$= \left| \langle \mathcal{F}(f - g), \frac{e^{-i\omega x}}{\sqrt{2\pi}} \rangle_{L^2[-\pi, \pi]} \right| \quad (3.5c)$$

$$\leq \|f - g\|_{L^2[-\pi, \pi]} \left\| \frac{e^{-i\omega x}}{\sqrt{2\pi}} \right\|_{L^2[-\pi, \pi]} \quad (3.5d)$$

$$= \|f - g\|_{L^2(\mathbb{R})} \quad (3.5e)$$

Other examples of RKHSs will be further explore as its relation to kernels are developed.

3.2.2 Reproducing Kernels

Riesz representation theorem is an extension, for Hilbert Spaces, of the classical isomorphism between a finite vector space \mathcal{V} and its dual \mathcal{V}^* , the space of linear functions on \mathcal{V} . It states that for every element $\phi \in \mathcal{H}^*$, where \mathcal{H}^* is the space *continuous* linear functionals from \mathcal{H} into \mathbb{R} (dual space), there exist a unique $f_\phi \in \mathcal{H}$, defined by:

$$\phi(g) = \langle g, f_\phi \rangle_{\mathcal{H}} \quad \forall g \in \mathcal{H}$$

As consequence, the evaluation functional δ_x has a representation on \mathcal{H} as k_x , the reproducing property:

$$f(x) = \delta_x(f) = \langle f, k_x \rangle_{\mathcal{H}} \quad \forall f \in \mathcal{H}$$

The important idea of pointwise convergence can be recovered:

$$|f(x) - g(x)| = |\delta_x(f - g)| \quad (3.6a)$$

$$= |\langle f - g, k_x \rangle_{\mathcal{H}}| \quad (3.6b)$$

$$\leq \|f - g\|_{\mathcal{H}} \|k_x\|_{\mathcal{H}}, \quad (3.6c)$$

where Cauchy-Schwarz inequality was used on line (3.6c) and $\|k_x\|_{\mathcal{H}}$ acts as a scaling factor the closeness at each specific x .

The evaluation functional represented in \mathcal{H} as k_x can be seen as a function itself. As such, its evaluation at every point y of \mathcal{X} point construct a two-variable function, the kernel:

$$k_x(y) = K(x, y) = \langle k_x, k_y \rangle_{\mathcal{H}} \quad (3.7)$$

The kernel function $K : \mathcal{X} \times \mathcal{X} \rightarrow \mathbb{R}$ is symmetric (because this is the real case) and positive definite as direct consequence of inner product definition. The converse, however, is a result of the Moore-Aronszajn theorem which says that for every symmetric positive definite function $K(\bullet, \bullet)$ (kernel) on $\mathcal{X} \times \mathcal{X}$ there is a unique Hilbert space \mathcal{H} of functions (RKHS) on \mathcal{X} for which K is a reproducing kernel. The reproducing property of the kernel is:

$$f(x) = \langle K(x, \bullet), f \rangle_{\mathcal{H}} \quad f \in \mathcal{H} \quad (3.8)$$

Examples of common used kernels:

- Gaussian Kernel/Radial Basis Function Kernel (RBF)

$$K(x, y) = e^{-\gamma \|x-y\|^2} \quad \gamma \in \mathbb{R}^+ \quad (3.9)$$

- Laplacian Kernel

$$K(x, y) = e^{-\lambda \|x-y\|} \quad \lambda \in \mathbb{R}^+$$

- PW_{π} Kernel (the bandlimited $L^2(\mathbb{R})$ space, see 3.2.1)

$$K(x, y) = \frac{\sin \pi(x-y)}{\pi(x-y)}$$

- Linear Kernel

$$K(x, y) = \langle x, y \rangle$$

- Polynomial Kernel

$$K(x, y) = (\gamma \langle x, y \rangle + 1)^n \quad \gamma \in \mathbb{R}, n \in \mathbb{N}^+$$

It is possible to operate with kernels and generate new valid kernels. If K_1, K_2 are kernels for \mathcal{H}_1 and \mathcal{H}_2 , respectively, then for any $\alpha, \beta \in \mathbb{R}_{\geq 0}$ it is possible to construct $K = \alpha K_1 + \beta K_2$ as a kernel for the RKHS $\mathcal{H} = \alpha \mathcal{H}_1 + \beta \mathcal{H}_2 = \{\alpha f_1 + \beta f_2 | f_1 \in \mathcal{H}_1, f_2 \in \mathcal{H}_2\}$. Kernel products are valid even for functions acting on different sets, that is, $K_1 : \mathcal{X} \times \mathcal{X} \rightarrow \mathbb{R}$ and $K_2 : \mathcal{Y} \times \mathcal{Y} \rightarrow \mathbb{R}$ define $K : (\mathcal{X} \times \mathcal{Y}) \times (\mathcal{X} \times \mathcal{Y}) \rightarrow \mathbb{R}$ as

$K((x, y), (x', y')) = K_1(x, x')K_2(y, y')$ with the RKHS $\mathcal{H} \cong \mathcal{H}_1 \otimes \mathcal{H}_2$, having $\mathcal{X} = \mathcal{Y}$ as a special case.

3.2.3 Feature Maps

A feature map is a map φ from a set $\mathcal{X} \neq \emptyset$ to a Hilbert space \mathcal{H} , the feature space. Any feature map can define a RKHS through the kernel:

$$K(x, y) = \langle \varphi(x), \varphi(y) \rangle_{\mathcal{H}} \quad x, y \in \mathcal{X} \quad (3.10)$$

For example, if \mathcal{X} is already a RKHS by itself, then feature map $\varphi(x) = x$ reconstruct the Linear Kernel. Also, a sequence of functions $f_i \in \mathbb{R}^{\mathcal{X}}, \forall i \in \mathbb{N}$ that $\{f_i(x)\} \in \ell^2, \forall x \in \mathcal{X}$ are themselves a feature map $\varphi(x) = \{f_i(x)\}$ with kernel:

$$K(x, y) = \sum_{i=1}^{\infty} f_i(x)f_i(y)$$

The converse, however, is not unique. Given a kernel there are multiple feature maps that can generate it. A simple example is $K(x, y) = 2xy$ with $\mathcal{X} = \mathbb{R}$, this kernel can also be generated by:

$$K(x, y) = \begin{bmatrix} x \\ x \end{bmatrix} \cdot \begin{bmatrix} y \\ y \end{bmatrix}$$

In the first case $\varphi_1(x) = x\sqrt{2} \in \mathbb{R}$, while in the second $\varphi_2(x) = \begin{bmatrix} x \\ x \end{bmatrix} \in \mathbb{R}^2$. Standard ways of finding and approximating feature maps will be discussed in the next sections.

3.3 Probabilistic Regression

Probabilistic regression is similar to classification, both infer properties of a sample based on previous information. However, instead of giving a definite answer for which class an element belongs, probabilistic regression gives the probability for such a classification [62]. More formally, a training set is a sequence of n pairs $\{(x_i, y_i) \mid i = 1, \dots, n\}$, where x_i and y_i are samples drawn from random variables X and Y , respectively, with joint probability distribution $\Pr(X, Y)$ [63]. From this training set, a conditioning probability $\Pr(Y|X = x)$ has to be estimated.

The special case where Y is a Bernoulli random variable, i.e. a binary variable, is called binary regression. It is the single most important regression for mapping, as such, no other kind is explored in this thesis.

3.3.1 Binary Logistic Regression

A binary regression dependent variable $Y \in \{-1, 1\}$ (or some set of equal cardinality like $\{0, 1\}$) has two possible estimations that are related by $\Pr(Y = 1|X = x) + \Pr(Y = -1|X = x) = 1$. As such, the conditional probability can be denoted

$$p(x) = \Pr(Y = 1|X = x)$$

The probability for $Y = -1$ can be recovered from $P(Y = -1|X = x) = 1 - p(x)$. The linear logistic model [2] $p(x; \mathbf{w})$ for $x \in \mathbb{R}^d$, with $\mathbf{w} \in \mathbb{R}^d$ as explicit parameter:

$$p(x; \mathbf{w}) = \frac{1}{1 + \exp(-\mathbf{w} \cdot x)} \quad (3.11)$$

The rationale behind the model is that the function $(1 + \exp(-\alpha))^{-1}$ is a bijection $\mathbb{R} \rightarrow (0, 1)$ [63]. Ensuring that the model is a probabilistic distribution.

The classical regression theory requires a loss function \mathcal{C} and minimizes an empirical risk over some space of functions $R[f] = \mathbb{E}(\mathcal{C}(X, Y, f(X)))$ [62], where $\mathbb{E}(\bullet)$ is the expected value. The estimation of f from samples (x_i, y_i) uses a regularized version:

$$R_{\text{reg}}[f] = \frac{1}{n} \sum_{i=1}^n \mathcal{C}(x_i, y_i, f(x_i)) + \lambda \mathcal{S}[f], \quad (3.12)$$

where $\lambda > 0$ and $\mathcal{S}[\bullet]$ stabilization (regularization) term, as the minimization problem is typically ill-posed [62]. On normed spaces usually $\mathcal{S}[f] = g(\|f\|)$, where $g(\bullet)$ is a monotonically increasing function. With proper adjustment of λ , the $1/n$ factor might be ignored without changing the minimizing function. The loss function \mathcal{C} is problem dependent and for binary regression a typical negative log likelihood (NLL) is used

$$\mathcal{C}(x, y, p(x)) = -\log \Pr(Y = y|X = x) = \begin{cases} -\log p(x) & y = 1 \\ -\log(1 - p(x)) & y = -1 \end{cases} \quad (3.13)$$

For a linear logistic model, one uses (3.11) on (3.13) and substitutes back into (3.12). Thus the regularized negative log likelihood empirical risk simplifies to a d dimensional minimization:

$$\text{NLL}_{\text{reg}}(\mathbf{w}) = \sum_{i=1}^n \log(1 + \exp(-y_i \mathbf{w} \cdot x_i)) + \lambda \mathcal{S}(\mathbf{w}). \quad (3.14)$$

Reasonable choices for $\mathcal{S}(\bullet)$ are the ℓ_1 norm (LASSO) $\mathcal{S}(\mathbf{w}) = \|\mathbf{w}\|_1$ or elastic net, a combination of ℓ_1 (LASSO) and squared ℓ_2 norms (ridge), $\mathcal{S}(\mathbf{w}) = \alpha_1 \|\mathbf{w}\|_1 + \alpha_2 \|\mathbf{w}\|_2^2$, where $\alpha_1 + \alpha_2 = 1$, $\alpha_1, \alpha_2 \in [0, 1]$ [64].

Although it is an applicable setting for simple situations, it is not expected to perform well for classification/regression of point on a 3D environment as $x \in \mathbb{R}^3$ and $\mathbf{w} \in \mathbb{R}^3$. A 3 real parameter \mathbf{w} is not enough to capture all the complexities of the environment. To keep the simplicity provided by linear, the alternative is to increase dimensionality using Hilbert Spaces.

3.3.2 Regression on Hilbert Spaces

Samples defined on a low dimensional space \mathcal{X} , e.g. \mathbb{R}^3 , can be raised to a high (possible infinite) dimensional space using a feature map $\varphi : \mathcal{X} \rightarrow \mathcal{H}$, where \mathcal{H} is hilbert space. This allow linear models to express more generic functions $f(x) = \langle \mathbf{w}, \varphi(x) \rangle_{\mathcal{H}}$ with $\mathbf{w} \in \mathcal{H}$, such a space of functions $f(x)$ is the actual RKHS with kernel define as in equation (3.10).

The linear logistic model from equation (3.11) lifted to the Hilbert Space \mathcal{H} is

$$p(x; \mathbf{w}) = \frac{1}{1 + \exp(-\langle \mathbf{w}, \varphi(x) \rangle_{\mathcal{H}})} \quad (3.15)$$

Thus, equation (3.14) for log likelihood empirical risk becomes⁴

$$\text{NLL}_{\text{reg}}(\mathbf{w}) = \sum_{i=1}^n \log(1 + \exp(-y_i \langle \mathbf{w}, \varphi(x_i) \rangle_{\mathcal{H}})) + \lambda \mathcal{S}(\mathbf{w}) \quad (3.16)$$

In practice, one chooses a kernel $K(x, y)$ with desired properties and find finite dimensional approximate features $\hat{\varphi}(x)$, such that $K(x, y) = \langle \varphi(x), \varphi(y) \rangle_{\mathcal{H}} \approx \hat{\varphi}(x) \cdot \hat{\varphi}(y)$. Non kernel specific methods for finding approximate features include sampling the Fourier transform of shift invariant kernels [65], i.e. $K(x, y) = k(x - y) = k(\delta)$, and Nyström method that projects the Gram matrix $\mathbf{G}_{ij} = K(x_i, x_j)$ of the sample points $\{x_i\}$ into some subset of these points and use this projection to approximate the feature maps [66].

⁴With appropriate adjustment of λ 's value, i.e. $\lambda = n\lambda_0$, the usual average $1/n$ for the summation can be dropped, as it keeps the same minimizer value of \mathbf{w} .

Chapter 4

Mapping

‘Would you tell me, please, which way
I ought to go from here?’
‘That depends a good deal on where
you want to get to,’ said the Cat.
‘I don’t much care where—’ said Alice.
‘Then it doesn’t matter which way you
go,’ said the Cat.

Alice’s Adventures in Wonderland
by Lewis Carroll

Mapping is not a predefined concept, there are different ways to think about mapping, it might depend on application and specific requirements. The unifying idea is a method to fuse and represent geometric information about a given environment. Nevertheless, the meaning of how to represent which information is a consequence of the application. Here, in this thesis, the objective is to have human-understandable map yet with a probabilistic interpretation of a 3D environment.

4.1 Map Representation

Classically maps are binary functions over the space. The binary choices of function’s range stand for fullness or emptiness of a point. Mapping (occupancy maps) is to construct a probability distribution over the set \mathcal{M}_d of all maps [1] on a given dimension d , i.e. $\mathcal{M}_d = \{\mathbf{m} \mid \mathbf{m} : \mathbb{R}^d \rightarrow \{0, 1\}\}$. The cardinality of such a set $|\mathcal{M}_d|$ is too big¹ to be tractable by exhaustion even considering computational discretization (finite precision), i.e. by individually assigning probabilities to each map.

Three approaches to this problem are presented here. One option is to consider conditional independence of spatial points and discretize the space even further, until

¹Side note: the actual mathematical cardinality is $\beth_2 = 2^{\mathfrak{c}}$ the cardinality the power set of the continuum, where \mathfrak{c} is the cardinality of the continuum

it becomes tractable. Another is to renounce the idea of binary maps and consider maps to be a collection of predefined objects. And lastly, keep the concept of binary maps, but to consider some restriction on the space of functions from which the map \mathbf{m} is drawn.

Despite their differences, all approaches describe marginal probabilities, which are functions over \mathbb{R}^d , instead of the probability for an actual map \mathbf{m} , whose domain is \mathcal{M}_d . Thus, for binary maps, the important quantity is $\Pr(\mathbf{m}(x^*) = 1)$ ², where $x^* \in \mathbb{R}^d$, and not $\Pr(\mathbf{m}^* = m_i)$, where $m_i \in \mathcal{M}_d$. When considering maps as collection of objects, the conditional probability is $\Pr(\mathbf{s}(\mathbf{l}_n) = \mathbf{s}_i)$, where $\mathbf{s}(\bullet)$ is the defining properties of an object \mathbf{l}_n , e.g. \mathbf{l}_n belongs to the set of segments and $\mathbf{s}(\mathbf{l}_n)$ gives its pair of endpoints.

4.1.1 Discrete Map

Discrete maps are also denominated *grid maps* because when discretizing each axis of a \mathbb{R}^d space the result is necessarily a grid. Originally developed for 2D maps [1], they were later extended to 3D maps in different ways.

3D grids

The first obvious extension was a 3D grid of cubes by discretizing a range of each direction on N elements. Reasoning that each cube still full or empty, the set of possible maps on a $N_1 \times N_2 \times N_3$ grid \mathbf{D} is $\bar{\mathcal{M}}_d = \{\mathbf{m} \mid \mathbf{m} : \mathbf{D} \rightarrow \{0, 1\}\}$. The cardinality of $|\bar{\mathcal{M}}_d| = 2^{N_1 \cdot N_2 \cdot N_3}$ is too big to store the probability of every element.

The simplifying assumption for 3D grid is the conditional independence of grid elements $\mathbf{m}(d_i)$ and $\mathbf{m}(d_j)$ on the sensors measurements \mathbf{z}_n , for $d_i \neq d_j$ where $d_i, d_j \in \mathbf{D}$. Therefore, the probability of a map become the product of the marginals:

$$\Pr(\mathbf{m} = m_i \mid \mathbf{z}_n) = \prod_{d \in \mathbf{D}} \Pr(\mathbf{m}(d) = m_i(d) \mid \mathbf{z}_n).$$

Writing marginals as $p_n(d) = \Pr(\mathbf{m}(d) = 1 \mid \mathbf{z}_n)$ keeps same information because $\Pr(\mathbf{m}(d) = m_i(d) \mid \mathbf{z}_n)$ equals $p_n(d)$ if $m_i(d) = 1$ and $1 - p_n(d)$ otherwise. The advantage is that it makes clearer that they can be stored and updated independently, and also that the number of stored elements is $|\mathbf{D}| = N_1 \cdot N_2 \cdot N_3$ ³. That might still be a lot, but with clever memory implementations like Octomaps [67], it can be manageable.

²The 1 here is completely arbitrary, it might as well be 0, as both probabilities are complementary.

³e.g. if $N_1 = N_2 = N_3 = 200$ for a 5cm resolution on cube with 10m edge, $|\mathbf{D}| = 8,000,000$ already.

Marginal probability computation on each cube is a direct application of Bayes rule⁴ (a Bayes filter) with a log-odds representation for better faster computation, known as occupancy in this context [1]:

$$l_n(d) = l_{n-1}(d) + \mathbf{inverse_sensor}(d, z_n) - l_0(d), \quad (4.1)$$

where $l_n(d)$ is the log-odds representation of $p_n(d)$, the n th estimate after all previous n sensor measurements \mathbf{z}_n , including the last one z_n .

$$l_n(d) = \log \frac{p_n(d)}{1 - p_n(d)}.$$

The *prior* of the occupancy is $l_0(d)$, log-odds of the *prior* probability $p_0(d)$. Defining $\mathbf{inverse_sensor}(d, z_n) = \Pr(\mathbf{m}(d) = 1 \mid z_n)$, it is the probability of fullness for a grid element d given **only** the last measurement z_n , it can be interpreted as inference from the sensor response, justifying the name.

THRUN *et al.* [1] suggests to abandon independency between grid elements. To archive that, Thrun employs a forward sensor model, instead of an **inverse_sensor**, and uses optimization algorithm Expectation Maximization (EM) on the marginal to find the best fit. It is successful on solving “conflicts” between sonar responses when, because of a wide beamwidth, the same region appears to be full and empty depending on viewpoint.

Another, not so well explored, approach for calculating the marginal probability for grid elements comes from Evidential Theory. Evidential Theory, a.k.a. Dempster-Shafer theory (DST), is a mathematical theory of evidence, assigning “probabilities” (belief mass) to all non-empty elements of the power set of events. On the binary $\{0, 1\}$ case, the three non-empty subsets are 0,1,0, 1 standing for evidence of emptiness, fullness or both, which “probabilities” add to one. Consequently yielding to two maps, one for fullness other for emptiness. In DTS the actual probability (in the classical sense) appears as lower and upper bounds (Plausability and Belief), allowing ignorance to be modeled adequately. The 2D case was explored by PAGAC *et al.* [68], their article also further describes DTS.

Grid based algorithms on 3D environments suffer from their high number of grid elements, the next model try to avoid this problem.

Elevation Maps

In an attempt to keep the grid to a reasonable size, elevation maps, or 2.5D maps, keep the discretization only on the 2 horizontal dimensions. The third dimension is represented as a height value assigned to each 2D discretization.

⁴ $\Pr(A \mid B) = \frac{\Pr(B \mid A) \Pr(A)}{\Pr(B)}.$

Some work on seabed reconstruction using sonars has been done by COIRAS *et al.* [69], COIRAS and GROEN [70]. They attempt to map by reconstructing a 2.5D surface through optimization on the height value of each grid element. That leads to information gain on local surface's reflectivity, an indication of its composition. However, the expectation-maximization method does not leave a direct probabilistic interpretation for the values.

Although elevation maps reduce memory requirements by not discretizing on the vertical axis, its elevation value is unique for each grid element. As such, it is not able to represent objects above the floor level, e.g. ceil, trees, caves, etc. That is addressed in the next option.

Multi Layer Surface - MLS

As a compromise between the last two solution, grid and elevation maps, Multi Layer Surface (MLS) was developed. It originates as elevation maps, but instead of having only one height per grid element, it splits into many layers of varying height, called *surface patches*.

When MLS was first proposed by TRIEBEL *et al.* [71], each surface patch of each grid element stored statistics as mean height and standard deviation. It was soon realized that a flat horizontal plane for a grid and a preferential vertical direction could be an issue for well describing statistical knowledge of the environment. Some extensions have already been suggested to address this matter, e.g. works of RIVADENEYRA and CAMPBELL [72] and SCHWENDNER [73].

4.1.2 Map of Features

A map can, in certain situations, be approximated by a collection of geometric objects, viz. line segments, circles, etc. This is specially true for structured environments [74] where walls and flat surfaces are easily found.

The 2D simplification, only considering the horizontal plan, was explored for underwater SLAM with Imagins Sonars by RIBAS *et al.* [75]. They used lines to represent an environment, with endpoints only for display purpose. Line extraction relied on polar the parametric space of lines (angle and distance to the origin) as on Hough Voting and extensions.

Besides only applied to 2D, a particular downside of the approach is its little generality. Generic, unstructured or complex environments are unhandleable.

4.1.3 Continuous Map

There is no need for discretization on space if some restrictions are applied to the space of function of maps. Formally that means $\tilde{\mathcal{M}}_d \subseteq \mathcal{V} \cap \mathcal{M}_d$, where \mathcal{V} is some restricted space of functions, e.g. continuous compact supported, and \mathcal{M}_d as defined in Section 4.1. In practice the restriction is not directly applied to the space of functions, instead it is enforced on the probability distribution, such that functions outside $\tilde{\mathcal{M}}_d$ have zero probability.

A marginal probability for continuous map evaluates at every point in \mathbb{R}^d , not in some discretized space as for 3D grids presented in Section 4.1.1. The marginals shall then be written as $p(x) = \Pr(\mathbf{m}(x) = 1)$ for $x \in \mathbb{R}^d$.

Gaussian Process Occupancy Maps - GPOM

Possibly the first succesful attempt to have a continuous map was the Gaussian Process Occupancy Maps (GPOM) by O'CALLAGHAN and RAMOS [76], as noted by the author there were previous attempts, but they lacked computability or did not truly represent occupancy. GPOM's method apply learning techniques, Gaussian Process, to estimate the best marginal for a family of functions $p(x) = \Phi(\bullet)$, where Φ is the cumulative unit Gaussian. Details of the learning process are numerous and complex, for the interested reader it is suggested to check the original paper. GPOM was already applied to 3D environments for path planning of a 6DOF Rotary Unmanned Aerial Vehicle (RUAV) using laser sensors⁵ [77].

Following ideas from GPOM, Hilbert Maps were proposed as a less computationally expensive alternative for continuous maps. It is also able to naturally account for spatial correlations and handle noise, but while GPOM scales cubically with data size, Hilbert Maps can be updated in linear time. Hilbert Maps is yet much simpler to implement and it was the chosen alternative for sonar reconstruction on this work. It suits well the task, as most of imaging sonar drawbacks are its noise and wide beamwidth.

Hilbert Maps

Hilbert Maps is a recent development by RAMOS and OTT [2], from 2016. It was implemented on the 2D case, on a laser sensor setting. This thesis applies the method to 3D environment with sonar, imaging sonar especially. Most of the mathematical machinery necessary was described in Chapter 3, however some details still to be presented.

⁵ $\Phi(x) = \frac{1}{\sqrt{2\pi}} \int_{-\infty}^x e^{-t^2/2} dt.$

Marginal probabilities are assumed to be linear logistic as in equation (3.15):

$$p(x; \mathbf{w}) = \frac{1}{1 + \exp(-\langle \mathbf{w}, \varphi(x) \rangle_{\mathcal{H}})},$$

where $\mathbf{w}, \varphi(x) \in \mathcal{H}$, \mathcal{H} a Hilbert space that generates a RKHS with kernel $K(x, y) = \langle \varphi(x), \varphi(y) \rangle_{\mathcal{H}}$. As long range correlations are not expected, a suitable kernel choice is the RBF defined on equation (3.9):

$$K(x, y) = e^{-\gamma \|x-y\|^2} \quad \gamma \in \mathbb{R}^+$$

The features $\varphi(x)$ are approximated as Nyström features, other methods did not show results as good [2]. Approximations were discussed in Section 3.3.2. Nyström features are sample dependent, given set of n “inducing” points $\nu_i \in \mathbb{R}^d$, $i = 1 \dots n$ chosen (possibly random) on the region being mapped, it is calculated as:

$$\hat{\varphi}(x) = \sqrt{1/\Lambda \mathbf{Q}^T} \hat{K}(x), \quad (4.2)$$

where $\mathbf{G} = \mathbf{Q} \Lambda \mathbf{Q}^T$ is the spectral decomposition of the Gram matrix of the “inducing” points, $\mathbf{G}_{ij} = K(\nu_i, \nu_j)$, and $\hat{K}_i(x) = K(x, \nu_i)$ is a column vector. After this finite approximations, $\mathbf{w} \in \mathbb{R}^n$ and equation (3.15) becomes:

$$p(x; \mathbf{w}) = \frac{1}{1 + \exp(-\mathbf{w} \cdot \hat{\varphi}(x))}, \quad (4.3)$$

and the negative log likelihood - NLL - regression, from equation (3.16) becomes:

$$\text{NLL}_{\text{reg}}(\mathbf{w}) = \sum_{i=1}^n \log(1 + \exp(-y_i \mathbf{w} \cdot \hat{\varphi}(x_i))) + \lambda \mathcal{S}(\mathbf{w}), \quad (4.4)$$

where (y_i, x_i) are the sample points and $\mathcal{S}(\bullet)$ an elastic-net regularizer, described on the context of logistic regression of Section 3.3.1:

$$\mathcal{S}(\mathbf{w}) = \alpha_1 \|\mathbf{w}\|_1 + \alpha_2 \|\mathbf{w}\|_2^2, \quad (4.5)$$

with $\alpha_1 + \alpha_2 = 1$, $\alpha_1, \alpha_2 \in [0, 1]$.

Minimization of $\text{NLL}_{\text{reg}}(\mathbf{w})$ gives a representation of the map as a n parameter vector \mathbf{w} . It can then be evaluated at any point with equation (4.3). The minimization step is solved iteratively as a learning process, discussed further ahead, which is naturally an online process.

4.2 Inverse Sonar Model

Methods that do not use Expectation-Maximization (EM), as some of those described in Sections 4.1.1, usually require some form of inversion of the sensor model. This is a way to characterize the environment from a sensor response.

In the context of grid maps, it appears as a conditional probability on the measurement, i.e. $\text{inverse_sensor}(d, z_n) = \Pr(\mathbf{m}(d) = 1 \mid z_n)$ in equation (4.1). For sonars, it is generally considered as a constant value for grid elements inside an occupied bin (see Figure 2.12) and another for those outside [1]. THRUN *et al.* [1] also create an inverse model by training a machine learning algorithm with generated responses.

The difference between an occupied bin and an empty one can be a simplistic bin-value threshold [1, 75, 78] or some more complex procedure, e.g. histograms.

4.2.1 Sonar on Feature Maps

For Hilbert Maps, only procedures for laser are already described, thus here a strategy is proposed for sonar responses. After defining the empty and full bins, there are three main differences between sonars and lasers: Sonars bins are volumetric; Lasers have a definite hit point, a full bin only means that there is something somewhere inside the bin; Sonars may have multiple full bins, on a beam, while lasers have only one hit.

Given the sonar/laser differences, it is suggested:

- I Sample the empty beam volume between the sonar and the first full bin.
- II Sample all full bin volumes, with a possible different sample density.

A beam volume is a frustum of a sphere, a region between the simple concept of aperture angles (see Section 2.1.2) and within a range of distances given by the bin. The sample density used was uniform on the volume, because it is a guide for the expected echo point within the bin and there is no obvious privileged point.

The rationale behind ignoring all empty bins after the first full bin is to avoid considering shadow zones as empty regions, i.e. acoustic shadows of the first echo. As empty regions means no echo anywhere inside the bin, they are actually the most important information provided by the sonar. Each sample from the empty beam volume is evaluated to the feature map and passed to the learning algorithm. However, full bins indicate an echo somewhere within the bin. Thus a whole collection of samples from a full bin are embedded to the Hilbert Space as a distribution [2, 79]:

$$\hat{\varphi}(\mathbb{P}) = \frac{1}{n} \sum_{i=1}^n \hat{\varphi}(x_i), \quad (4.6)$$

where \mathbb{P} is the original distribution from where n samples x_i are drawn. In the machine learning setting, this $\hat{\varphi}(\mathbb{P})$ can be considered more than once, if the certainty is higher, as it will be commented in the next section.

4.3 Map Learning

Map learning is an iterative optimization process to find the \mathbf{w} that minimizes $\text{NLL}_{\text{reg}}(\mathbf{w})$, equation (4.4). As it is a convex function, gradient descent method would find it global minimum. The gradient of the objective function is:

$$\nabla \text{NLL}_{\text{reg}}(\mathbf{w}) = \sum_{i=1}^n -y_i \hat{\varphi}(x_i) (1 + \exp(y_i \mathbf{w} \cdot \hat{\varphi}(x_i)))^{-1} + \lambda \nabla \mathcal{S}(\mathbf{w}). \quad (4.7)$$

The gradient $\nabla \mathcal{S}(\mathbf{w})$ is calculated using sub-differentials, as the ℓ_1 part of an elastic-net $\mathcal{S}(\mathbf{w})$, equation (4.5), is non-differentiable at $\mathbf{w} = \mathbf{0}$.

The gradient descent method generates a sequence of approximated values for \mathbf{w} by descending on the gradient direction:

$$\mathbf{w}_{t+1} = \mathbf{w}_t - \eta \nabla \text{NLL}_{\text{reg}}(\mathbf{w}_t), \quad (4.8)$$

where $\eta \in \mathbb{R}^+$ is a step value and \mathbf{w}_t is a sequence of approximations. The issue with this approach is the cost of computing $\nabla \text{NLL}_{\text{reg}}(\mathbf{w})$ for a whole map, the summation of equation (4.7) ranges over all sampled points from all beams from all measurements, with sampling as in Section 4.2, and it is computed at every step of \mathbf{w}_t .

4.3.1 Stochastic Gradient Descent - SGD

To overcome the sampling size issue of gradient descent, stochastic gradient descent proposes the use of a single, or small batch, of samples at a time. One first shuffle the training samples [80] then directly update \mathbf{w}_t as:

$$\mathbf{w}_{t+1} = \mathbf{w}_t - \eta_t \nabla \text{NLL}_{\text{reg}}(\mathbf{w}_t; (y_t, x_t)), \quad (4.9a)$$

$$\nabla \text{NLL}_{\text{reg}}(\mathbf{w}_t; (y_t, x_t)) = -y_t \hat{\varphi}(x_t) (1 + \exp(y_t \mathbf{w} \cdot \hat{\varphi}(x_t)))^{-1} + \lambda \nabla \mathcal{S}(\mathbf{w}), \quad (4.9b)$$

where (y_t, x_t) are the shuffled version of (y_i, x_i) . The mini-batch variation [81] of this method takes partition the set of samples $\sqcup_k I_k = \{(y_i, x_i) | i = 1 \dots n\}$ and shuffle, then the update equation becomes:

$$\mathbf{w}_{t+1} = \mathbf{w}_t - \eta_t \nabla \text{NLL}_{\text{reg}}(\mathbf{w}_t; I_t) \quad (4.10a)$$

$$\nabla \text{NLL}_{\text{reg}}(\mathbf{w}_t; I_t) = \sum_{(y_i, x_i) \in I_t} -y_t \hat{\varphi}(x_i) (1 + \exp(y_i \mathbf{w} \cdot \hat{\varphi}(x_i)))^{-1} + \lambda \nabla \mathcal{S}(\mathbf{w}) \quad (4.10b)$$

The algorithm is guaranteed to converge (under mild conditions BOTTOU [80]), given that $\sum_t \eta_t^2 < \infty$ and $\sum_t \eta_t = \infty$. A classic choice for η_t is

$$\eta_t = \frac{\eta_0}{1 + t/n}. \quad (4.11)$$

Where η_0 is an initial step determined from a small sample and n is the number of samples. Variations of this form also are common, RAMOS and OTT [2] provides another choice:

$$\eta_t = \frac{1}{\lambda \alpha_2 (t_0 + t)}.$$

Where λ is the regulator gain, equation (4.10a), α_2 is the ℓ_2 elastic-net gain, equation (4.5), and t_0 is chosen from a small sample test. However, TSURUOKA *et al.* [82] adopts an exponential decay for η_t , which is not compliant with theoretical requirements, and they had a better result than using equation (4.11). The reason provided was that an harmonic progression decays too fast at the beginning and too slowly at the end. As a trade-off, this work employs a theoretically valid step that do not suffer from the aforementioned limitations:

$$\eta_t = \frac{\eta_0}{2} \left(\frac{1}{(1 + t/n) \log_n(n + t)} + k_1 e^{-t/n} \right), \quad (4.12)$$

where η_0 , similarly to the classical case, is an initial step. The rationale is to accommodate a slower decay at the beginning, dictated by the exponential component, and faster at the end without losing the divergence, as $\sum_x x \log x$ still divergent. Faster decaying end rates can always be found, if needed.

4.4 Implementation

4.4.1 Algorithm

The implemented algorithm receives as input a sequence of sonar positions \mathbf{P}_k and its respective sonar responses, that is a sequence of beams $\mathbf{b}_j^{(k)}$ containing bearing and bins values. The procedure goes as illustrated in Algorithm 3.

In the description of the algorithm $\nabla \text{NLL}_{\text{reg}}(\mathbf{w}_t; \text{feats})$ has a slightly different meaning:

$$\nabla \text{NLL}_{\text{reg}}(\mathbf{w}_t; \text{feats}) = \sum_{\hat{\varphi} \in \text{feats}} -y_t \hat{\varphi} (1 + \exp(y_i \mathbf{w} \cdot \hat{\varphi}))^{-1} + \lambda \nabla \mathcal{S}(\mathbf{w})$$

Algorithm 3 Mapping

```
procedure MAPPING( $\mathbf{P}_k, \mathbf{b}_j^{(k)}$ )  
   $I_k = \{\mathbf{b}_j^{(k)} | j \in \mu\mathbb{N}\}$  ▷ Partitioning at every  $\mu$  beam  
   $\mathbf{w}_0 = \mathbf{0}$   
  for all  $\mathbf{P}_k$  do  
    for all  $\mathbf{b} \in I_k$  do  
       $\mathbf{b} = \text{threshold}(\mathbf{b})$  ▷ Classify empty/full, Section 4.2  
       $e_i = \text{empty\_samples}(\mathbf{b})$  ▷ Sample first empty bins, Section 4.2.1  
       $f_i^{(z)} = \text{full\_samples}(\mathbf{b})$  ▷ Sample from every  $z$  full bin, Section 4.2.1  
       $\text{feats} = \{\}$  ▷ Empty set initialization  
      for all  $e_i$  do  
         $\text{feats} = \text{feats} \cup \{\hat{\varphi}(e_i)\}$  ▷ equation (4.2)  
      end for  
      for all  $f_i^{(z)}$  do  
         $\text{feats} = \text{feats} \cup \{\mathbb{E}_i[\hat{\varphi}(f_i^{(z)})]\}$  ▷ equation (4.6)  
      end for  
    end for  
     $\mathbf{w}_- = \eta_k \nabla \text{NLL}_{\text{reg}}(\mathbf{w}_t; \text{feats})$  ▷ equation (4.12) on a variant of (4.10a)  
  end for  
  return  $\mathbf{w}$   
end procedure
```

The platform used for carrying out numerical simulation was developed using Python programming language (<https://www.python.org/>). NumPy scientific library (<http://www.numpy.org/>) was employed for linear algebra manipulation. And Matplotlib library (<https://matplotlib.org/>) was used for the cross sectional plots.

4.4.2 Results

Although the algorithm generates a 3D representation of an environment, results displayed here are plane cuts of this reconstruction only for better appreciation. The environment considered here is the 4x5 semi-infinity box of section (2.3.1). There were used 3000 inducing points (dimension of the feature map approximation - Section 4.1.3) and 21 measurements from 7 different positions in 3 orthogonal orientations each from the sonar simulation. Different fractions of the number of beams were explored on three figures 4.1, 4.2 and 4.3, their axis obey the standard orientation. Colors represent the value of the occupancy $p(x; \mathbf{w})$.

Figure 4.4 shows a different setup, it used only one sonar position oriented in 3 different ways. The figure is divided into two pairs of images, each using a different fraction of the total number of beams.

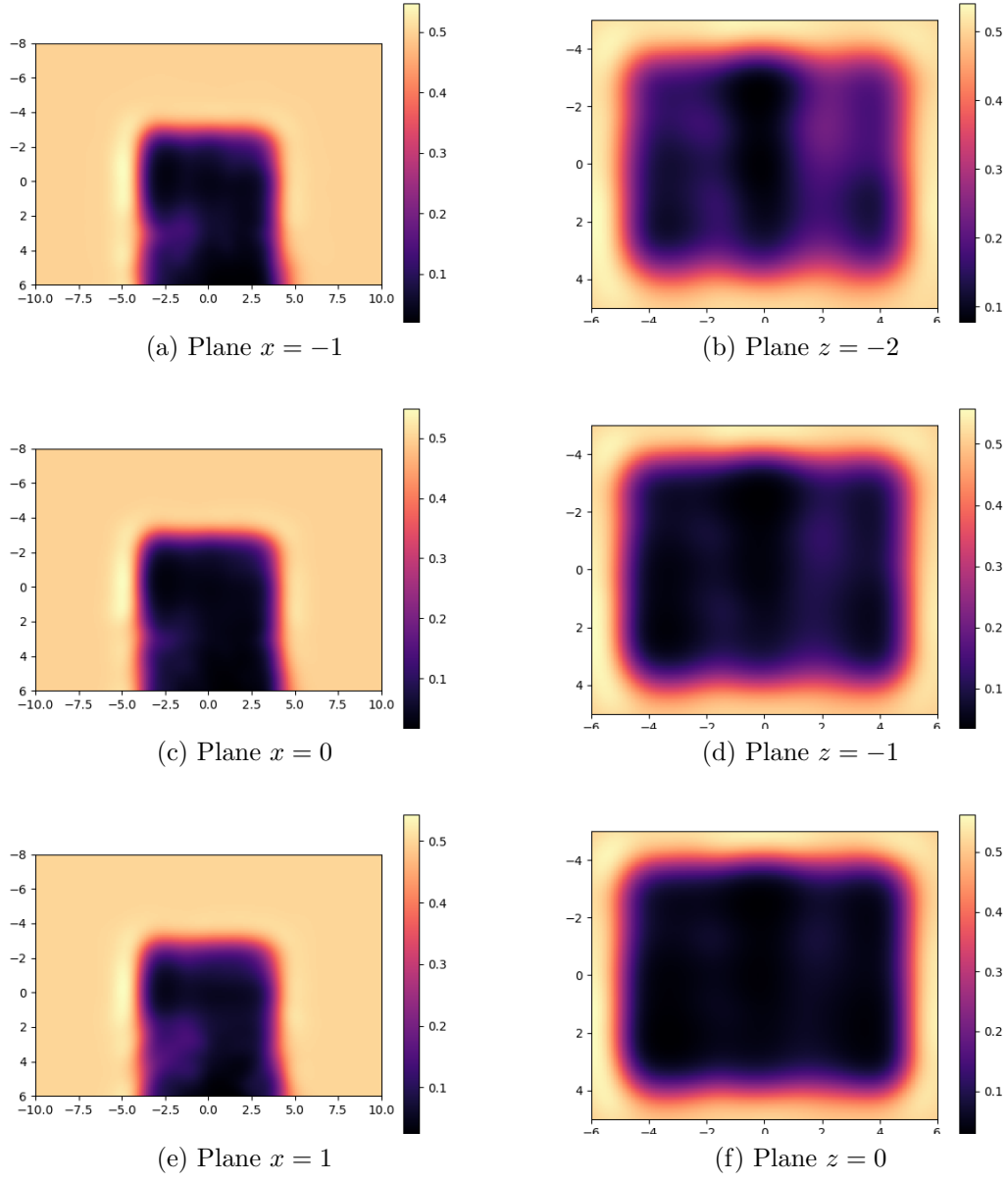


Figure 4.1: Mapping with 10% of available beams.

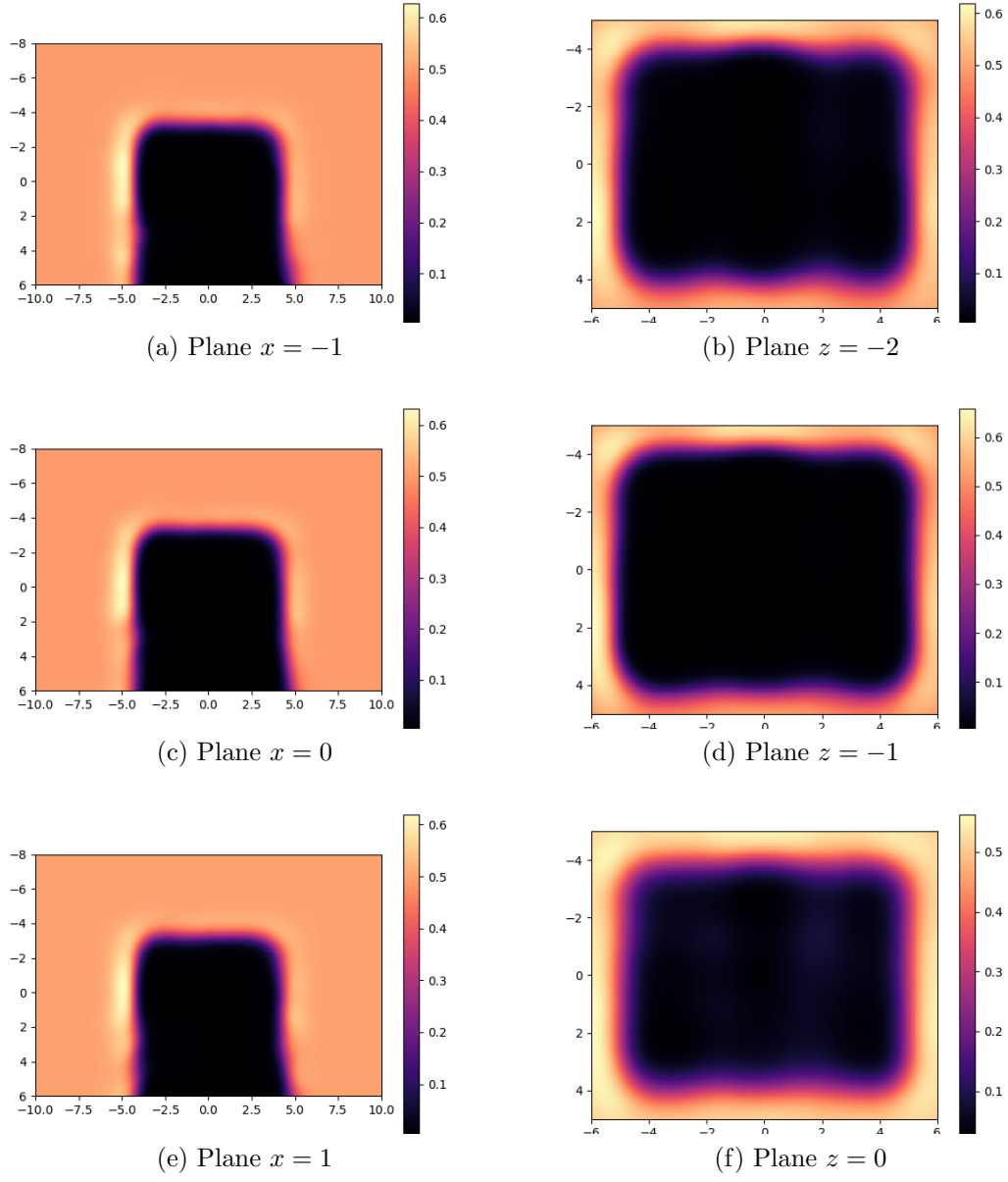


Figure 4.2: Mapping with 30% of available beams.

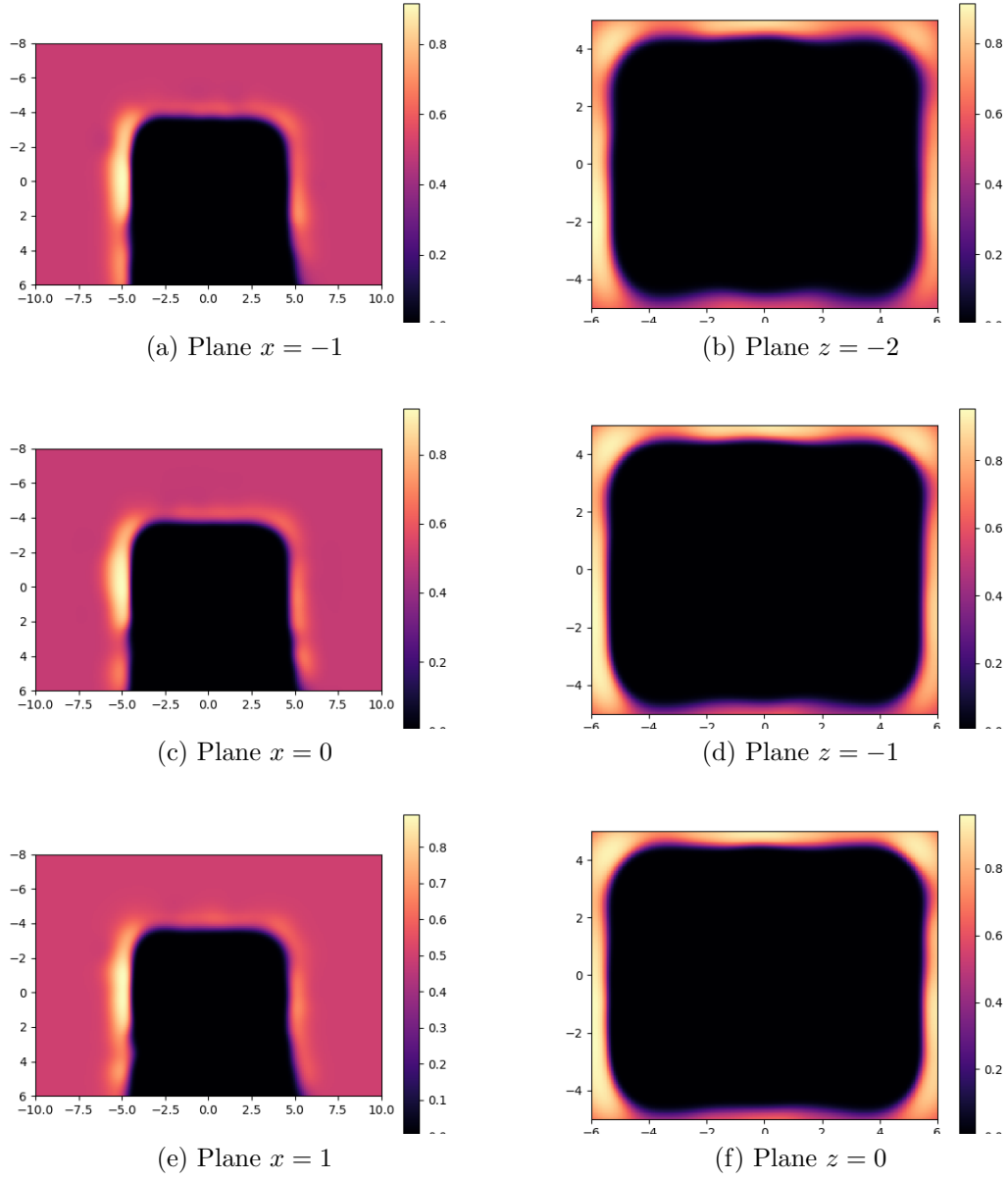


Figure 4.3: Mapping with 100% of available beams, with double pass over samples.

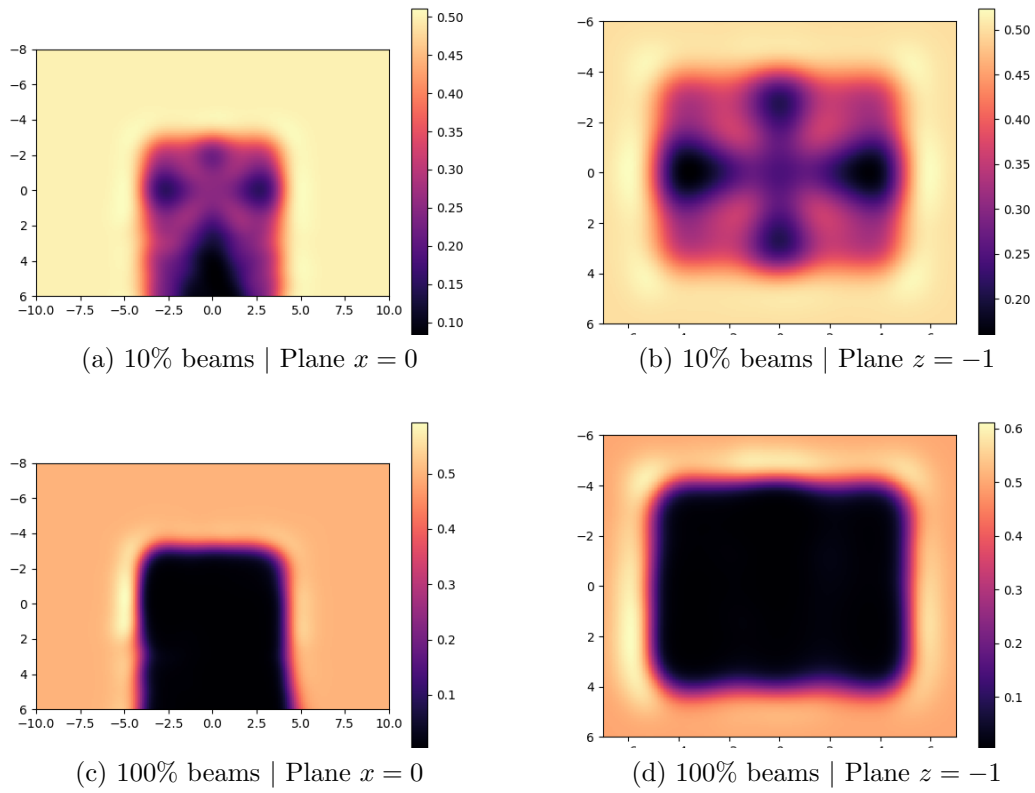


Figure 4.4: Mapping using only 1 position and 3 sonar orientations, with different number of used beams.

Chapter 5

Conclusion

All models are wrong, but some are useful.

George E. P. Box

The mapping for a single position using all beams is displayed in figure 5.1. This figure also contains a thin green line representing the ground truth for the box-like environment used as input to the simulator.

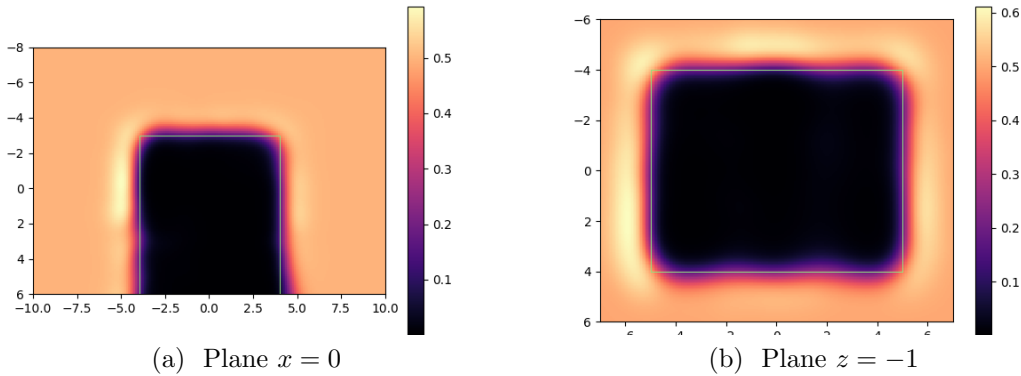


Figure 5.1: Mapping using only 1 position and 3 sonar orientations with ground truth as green lines.

Qualitatively, the empty region is almost perfectly reconstructed, with corners smoothed out. However the walls themselves are over a region of probability $\approx 35\%$. This low probability value can be explained as consequence of having a highly reliable information about emptiness in contrast with a diffuse measurement of occupied regions. Such a difference, together with a smooth kernel space may create a slow change between the regions, biased towards empty space. The smoothed corners may also be partially caused by the choice of kernel and its approximation.

Nevertheless, the Hibert Maps applied to the underwater problem manifest a depiction of the environment clear enough for humans to read and still have a promising

result for localization. The maximum error between the ground truth and the half probability region was about 45cm (Fig.5.2)

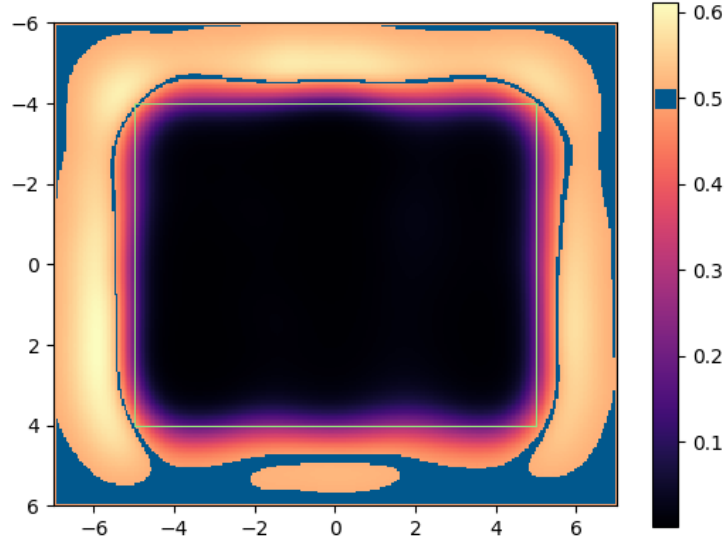


Figure 5.2: Blue region is the half probability region and green lines represent ground truth.

5.1 Future Works

On the simulation side, resonable next steps include implementing a more complex BDRF to emulate more realistic materials, although that depends on measurements which creates an extra difficulty. Also experimentation with Metropolis Transport similar methods that could improve less sharp shadows and caustics depiction.

The mapping with Hilbert maps is a parametric method, thus automatic selection is a simple incremental change, which may also include other feature approximations. A post processing step could be also envisioned, an optimization step, with a forward sonar model (simulation), to generate sharper corners and retrieve information about the surroundings, similar to elevation maps optimization (section 4.1.2).

Bibliography

- [1] THRUN, S., BURGARD, W., FOX, D. *Probabilistic Robotics*. Intelligent robotics and autonomous agents. MIT Press, 2005. ISBN: 9780262201629. Available at: <<https://books.google.com.br/books?id=2Zn6AQAAQBAJ>>.
- [2] RAMOS, F., OTT, L. “Hilbert maps: scalable continuous occupancy mapping with stochastic gradient descent”, *The International Journal of Robotics Research*, v. 35, n. 14, pp. 1717–1730, 2016.
- [3] ETTER, P. C. *Underwater Acoustic Modeling and Simulation, Fourth Edition*. CRC Press, feb 2013. ISBN: 978-1-4665-6493-0. doi: 10.1201/b13906. Available at: <<http://www.crcnetbase.com/doi/book/10.1201/b13906>>.
- [4] FEYNMAN, R. P., LEIGHTON, R. B., SANDS, M. *The Feynman lectures on physics, Vol. I: The new millennium edition: mainly mechanics, radiation, and heat*, v. 1. Basic Books, 2015.
- [5] BRUNEAU, M. *Fundamentals of Acoustics*. ISTE, 2006.
- [6] FILIPPI, P., BERGASSOLI, A., HABAULT, D., et al. *Acoustics: basic physics, theory, and methods*. Academic Press, 1998.
- [7] LURTON, X. *An Introduction to Underwater Acoustics: Principles and Applications*. Springer Praxis Publishing, London, UK, 2010.
- [8] FAHY, F., WALKER, J. *Fundamentals of Noise and Vibration*. Taylor & Francis, 1998. ISBN: 9780419241805. Available at: <<https://books.google.com.br/books?id=lo4wUkHm9j0C>>.
- [9] D’AMICO, A., PITTENGER, R. *A brief history of active sonar*. Technical report, DTIC Document, 2009.
- [10] CHAUDHARI, M. “Chirp Sonar and Electrical Resistivity Imaging survey for integrity of concrete lining in a Hydrel Channel”, *JOURNAL OF INDIAN GEOPHYSICAL UNION*, v. 19, n. 2, pp. 167–174, 2015.

- [11] B.I.LEMBRIKOV, D. *Chirped Gaussian Pulses*. Technical report, Holon Academic Institute of Technology, 2005.
- [12] “Sidescan Sonar Beamwidth”. 2005. Application Note.
- [13] CLAPP, M. A., ETIENNE-CUMMINGS, R. “Single ping-multiple measurements: Sonar bearing angle estimation using spatiotemporal frequency filters”, *IEEE Transactions on Circuits and Systems I: Regular Papers*, v. 53, n. 4, pp. 769–783, 2006.
- [14] KNEIPFER, R. R. *Sonar Beamforming-An Overview Of Its History and Status*. Technical report, DTIC Document, 1992.
- [15] CHU, D., HUFNAGLE, L. C. “Time varying gain (TVG) measurements of a multibeam echo sounder for applications to quantitative acoustics”. In: *OCEANS 2006*, pp. 1–5. IEEE, 2006.
- [16] CHEW, J. L., CHITRE, M. “Object detection with sector scanning sonar”. In: *Oceans-San Diego, 2013*, pp. 1–8. IEEE, 2013.
- [17] DOBSON, C. “Introducing Sonar Technology as a Tool for Underwater Cave Surveying”, *BCRA Cave Radio & Electronics Group*, v. 94, pp. 20–23, 2016.
- [18] JENSEN, F., KUPERMAN, W., PORTER, M., et al. *Computational Ocean Acoustics*. Modern Acoustics and Signal Processing. Springer New York, 2011. ISBN: 9781441986788.
- [19] FUNKHOUSER, T., TSINGOS, N., JOT, J.-M. “Survey of methods for modeling sound propagation in interactive virtual environment systems”. 2003.
- [20] URICK, R. J. *Sound propagation in the sea*. Technical report, DARPA, 1979.
- [21] DEINES, E., BERTRAM, M., MOHRING, J., et al. “Comparative visualization for wave-based and geometric acoustics”, *IEEE Transactions on Visualization and Computer Graphics*, v. 12, n. 5, pp. 1173–1180, 2006.
- [22] BUCKINGHAM, M. J. *Ocean-acoustic propagation models*. EUR-OP, 1992.
- [23] TORRES, J. C. *Modeling of high-frequency acoustic propagation in shallow water*. Ph.D. Thesis, Monterey California. Naval Postgraduate School, 2007.
- [24] STATES, N. D. R. C. U. *Physics of Sound in the Sea*. Department of the Navy, Headquarters Naval Material Command, 1969.

- [25] DESANTO, J. *Scalar Wave Theory: Green's Functions and Applications*. Springer Series on Wave Phenomena. Springer Berlin Heidelberg, 2012. ISBN: 9783642847387.
- [26] ABRAMOWITZ, M., STEGUN, I. A. *Handbook of mathematical functions: with formulas, graphs, and mathematical tables*, v. 55. Courier Corporation, 1964.
- [27] BAKER, M., SUTLIEF, S. “Green’s Functions in Physics Version”, 2003.
- [28] WORZEL, J., EWING, M., PEKERIS, C. *Propagation of Sound in the Ocean*. Geological Society of America Memoir. Geological Society of America, 1948. ISBN: 9780813710273. Available at: <<https://books.google.com.br/books?id=UWaGs8720DcC>>.
- [29] MILLER, T. E. *Real time bottom reverberation simulation in deep and shallow ocean environments*. Ph.D. Thesis, Massachusetts Institute of Technology and Woods Hole Oceanographic Institution, 2015.
- [30] BELL, J. M. “Application of optical ray tracing techniques to the simulation of sonar images”, *Optical Engineering*, v. 36, n. 6, pp. 1806–1813, 1997.
- [31] BARTELL, F. O., DERENIAK, E., WOLFE, W. “The theory and measurement of bidirectional reflectance distribution function (BRDF) and bidirectional transmittance distribution function (BTDF)”. In: *1980 Huntsville Technical Symposium*, pp. 154–160. International Society for Optics and Photonics, 1981.
- [32] RÖBER, N., KAMINSKI, U., MASUCH, M. “Ray acoustics using computer graphics technology”. In: *10th International Conference on Digital Audio Effects (DAFx-07)*, S, pp. 117–124. Citeseer, 2007.
- [33] BLAKE, V. S. “Remote sensing in underwater archaeology: Simulation of side scan sonar images using ray tracing techniques”, *BAR INTERNATIONAL SERIES*, v. 598, pp. 39–39, 1995.
- [34] DURANY, J., MATEOS, T., GARRIGA, A. “Analytical Computation of Acoustic Bidirectional Reflectance Distribution Functions”, *Open Journal of Acoustics*, v. 5, n. 04, pp. 207, 2015.
- [35] OF STANDARDS, U. S. N. B., NICODEMUS, F. E. *Geometrical considerations and nomenclature for reflectance*, v. 160. US Department of Commerce, National Bureau of Standards, 1977.

- [36] COX, T., D'ANTONIO, P. *Acoustic Absorbers and Diffusers: Theory, Design and Application*. Taylor & Francis, 2004. ISBN: 9780203492994. Available at: <<https://books.google.com.br/books?id=IDAuR3dn5ZsC>>.
- [37] COX, T. J., DALENBACK, B.-I., D'ANTONIO, P., et al. "A tutorial on scattering and diffusion coefficients for room acoustic surfaces", *Acta Acustica united with ACUSTICA*, v. 92, n. 1, pp. 1–15, 2006.
- [38] JONES, A. D., SENDT, J., DUNCAN, A. J., et al. "Modelling the acoustic reflection loss at the rough ocean surface". In: *Proceedings of ACOUSTICS*, pp. 23–25, 2009.
- [39] DUNN, F., HARTMANN, W., CAMPBELL, D., et al. *Springer handbook of acoustics*. Springer, 2015.
- [40] VORLÄNDER, M., MOMMERTZ, E. "Definition and measurement of random-incidence scattering coefficients", *Applied Acoustics*, v. 60, n. 2, pp. 187–199, 2000.
- [41] RINDEL, J. H. "Scattering in room acoustics and related activities in ISO and AES". In: *Proceedings of 17th International Congress on Acoustics, Rome, Italy, 2-7 September*, 2001.
- [42] SILTANEN, S., LOKKI, T., KIMINKI, S., et al. "The room acoustic rendering equation", *The Journal of the Acoustical Society of America*, v. 122, n. 3, pp. 1624–1635, 2007.
- [43] PHONG, B. T. "Illumination for computer generated pictures", *Communications of the ACM*, v. 18, n. 6, pp. 311–317, 1975.
- [44] TRACER, A. R. C., BEAM, G., MOA, Q., et al. "Outdoor Sound Propagation with". .
- [45] CHANDAK, A., ANTANI, L., TAYLOR, M., et al. "Fast and accurate geometric sound propagation using visibility computations", *Building Acoustics*, v. 18, n. 1-2, pp. 123–144, 2011.
- [46] MUNJAL, M., MECHEL, F., VORLÄNDER, M., et al. *Formulas of Acoustics*. Springer Berlin Heidelberg, 2013. ISBN: 9783662072967. Available at: <<https://books.google.com.br/books?id=At95BgAAQBAJ>>.
- [47] REIF, J. H., TYGAR, J., YOSHIDA, A. "Computability and complexity of ray tracing", *Discrete & Computational Geometry*, v. 11, n. 3, pp. 265–288, 1994.

- [48] BLAKEY, E. “Ray tracing—computing the incomputable?” *arXiv preprint arXiv:1404.0075*, 2014.
- [49] VEACH, E., GUIBAS, L. J. “Metropolis light transport”. In: *Proceedings of the 24th annual conference on Computer graphics and interactive techniques*, pp. 65–76. ACM Press/Addison-Wesley Publishing Co., 1997.
- [50] LESLIE, J., CHEESMAN, W. “An ultrasonic method of studying deterioration and cracking in concrete structures”, *Journal of the American Concrete Institute*, v. 21, n. 1, pp. 17–36, 1949.
- [51] BELL, J. M., LINNETT, L. “Simulation and analysis of synthetic sidescan sonar images”, *IEEE Proceedings-radar, sonar and navigation*, v. 144, n. 4, pp. 219–226, 1997.
- [52] COIRAS, E., RAMIREZ-MONTESINOS, A., GROEN, J. “GPU-based simulation of side-looking sonar images”. In: *OCEANS 2009-EUROPE*, pp. 1–6. IEEE, 2009.
- [53] MAUSSANG, F., CHANUSSOT, J., HÉTET, A., et al. “Mean–standard deviation representation of sonar images for echo detection: Application to SAS images”, *IEEE Journal of Oceanic Engineering*, v. 32, n. 4, pp. 956–970, 2007.
- [54] BELL, J., DARLINGTON, D., ELSTON, G. “Techniques for the physical modeling of the sonar image generation process”. In: *Proc. 1st Int. Symp. Physics Signal Image Processing (PSIP’99)*, pp. 66–72. Citeseer, 1999.
- [55] BORAWSKI, M., FORCZMAŃSKI, P. “Sonar image simulation by means of ray tracing and image processing”. In: *Enhanced methods in computer security, biometric and artificial intelligence systems*, Springer, pp. 209–214, 2005.
- [56] *Micron Sonar Product Manual*, 02 ed. Trittech International Ltd, . 0650-SOM-00003.
- [57] *Micron Modem Product Manual*, 02 ed. Trittech International Ltd, . 0630-SOM-00001.
- [58] YOUNG, N. *An introduction to Hilbert space*. 14th ed. The Edinburgh Building, Cambridge CB2 8RU, UK, Cambridge University Press, 2011.
- [59] HUNTER, J. K., NACHTERGAELE, B. *Applied Analysis*. Department of Mathematics, University of California, 2000.

- [60] BERLINET, A., THOMAS-AGNAN, C. *Reproducing kernel Hilbert spaces in probability and statistics*. Springer Science & Business Media, 2011.
- [61] TREFETHEN, L. N. *Finite difference and spectral methods for ordinary and partial differential equations*. Cornell University-Department of Computer Science and Center for Applied Mathematics, 1996.
- [62] JAAKKOLA, T. S., HAUSSLER, D. “Probabilistic kernel regression models.” In: *AISTATS*, 1999.
- [63] FRIEDMAN, J., HASTIE, T., TIBSHIRANI, R. *The elements of statistical learning*, v. 1. Springer series in statistics Springer, Berlin, 2001.
- [64] HASTIE, T., TIBSHIRANI, R., WAINWRIGHT, M. *Statistical learning with sparsity*. CRC press, 2015.
- [65] RAHIMI, A., RECHT, B., OTHERS. “Random Features for Large-Scale Kernel Machines.” In: *NIPS*, v. 3, p. 5, 2007.
- [66] WILLIAMS, C. K., SEEGER, M. “Using the Nyström method to speed up kernel machines”. In: *Proceedings of the 13th International Conference on Neural Information Processing Systems*, pp. 661–667. MIT press, 2000.
- [67] HORNUNG, A., WURM, K. M., BENNEWITZ, M., et al. “OctoMap: An efficient probabilistic 3D mapping framework based on octrees”, *Autonomous Robots*, v. 34, n. 3, pp. 189–206, 2013.
- [68] PAGAC, D., NEBOT, E. M., DURRANT-WHYTE, H. “An Evidential Approach to Map-Building for Autonomous Vehicles”, *IEEE Transactions on Robotics and Automation*, v. 14, No 4, n. 4, pp. 623–629, 1998.
- [69] COIRAS, E., PETILLOT, Y., LANE, D. M. “Multiresolution 3-D reconstruction from side-scan sonar images.” *IEEE transactions on image processing : a publication of the IEEE Signal Processing Society*, v. 16, n. 2, pp. 382–90, feb 2007. ISSN: 1057-7149.
- [70] COIRAS, E., GROEN, J. “Simulation and 3d reconstruction of sidelooking sonar images”, *Advances in sonar technology. IN-TECH*, , n. February, pp. 1–15, 2009.
- [71] TRIEBEL, R., PFAFF, P., BURGARD, W. “Multi-level surface maps for outdoor terrain mapping and loop closing”. In: *Intelligent Robots and Systems, 2006 IEEE/RSJ International Conference on*, pp. 2276–2282. IEEE, 2006.

- [72] RIVADENEYRA, C., CAMPBELL, M. “Probabilistic multi-level maps from LI-DAR data”, *The International Journal of Robotics Research*, v. 30, n. 12, pp. 1508–1526, 2011.
- [73] SCHWENDNER, J. *Embodied Localisation and Mapping*. Ph.D. Thesis, University of Bremen, 2013.
- [74] RIBAS, D., RIDAO, P., NEIRA, J., et al. “SLAM using an imaging sonar for partially structured underwater environments”, *IEEE International Conference on Intelligent Robots and Systems*, pp. 5040–5045, 2006. doi: 10.1109/IROS.2006.282532.
- [75] RIBAS, D., RIDAO, P., NEIRA, J. *Underwater SLAM for structured environments using an imaging sonar*, v. 65. Springer, 2010.
- [76] O’CALLAGHAN, S. T., RAMOS, F. T. “Gaussian process occupancy maps”, *The International Journal of Robotics Research*, v. 31, n. 1, pp. 42–62, 2012.
- [77] GAN, S. K., YANG, K., SUKKARIEH, S. “3d path planning for a rotary wing uav using a gaussian process occupancy map”. In: *Australasian Conference on Robotics and Automation (ACRA)*, 2009.
- [78] MORAVEC, H., ELFES, A. “High resolution maps from wide angle sonar”, *Proceedings. 1985 IEEE International Conference on Robotics and Automation*, 1985. doi: 10.1109/ROBOT.1985.1087316. Available at: <http://ieeexplore.ieee.org/xpls/abs/_all.jsp?arnumber=1087316>.
- [79] SONG, L., FUKUMIZU, K., GRETTON, A. “Kernel embeddings of conditional distributions: A unified kernel framework for nonparametric inference in graphical models”, *IEEE Signal Processing Magazine*, v. 30, n. 4, pp. 98–111, 2013.
- [80] BOTTOU, L. “Stochastic gradient descent tricks”. In: *Neural networks: Tricks of the trade*, Springer, pp. 421–436, 2012.
- [81] LI, M., ZHANG, T., CHEN, Y., et al. “Efficient mini-batch training for stochastic optimization”. In: *Proceedings of the 20th ACM SIGKDD international conference on Knowledge discovery and data mining*, pp. 661–670. ACM, 2014.
- [82] TSURUOKA, Y., TSUJII, J., ANANIADOU, S. “Stochastic gradient descent training for l1-regularized log-linear models with cumulative penalty”. In: *Proceedings of the Joint Conference of the 47th Annual Meeting of the*

ACL and the 4th International Joint Conference on Natural Language Processing of the AFNLP: Volume 1-Volume 1, pp. 477–485. Association for Computational Linguistics, 2009.